GFDL's CM2 Global Coupled Climate Models. Part I: Formulation and Simulation Characteristics

THOMAS L. DELWORTH,[a] ANTHONY J. BROCCOLI,[b] ANTHONY ROSATI,[a] RONALD J. STOUFFER,[a] V. BALAJI,[c] JOHN A. BEESLEY,[d] WILLIAM F. COOKE,[e,*] KEITH W. DIXON,[a] JOHN DUNNE,[a] K. A. DUNNE,[f] JEFFREY W. DURACHTA,[e,*] KIRSTEN L. FINDELL,[a] PAUL GINOUX,[a] ANAND GNANADESIKAN,[a] C. T. GORDON,[a] STEPHEN M. GRIFFIES,[a] RICH GUDGEL,[a] MATTHEW J. HARRISON,[a] ISAAC M. HELD,[a] RICHARD S. HEMLER,[a] LARRY W. HOROWITZ,[a] STEPHEN A. KLEIN,[a,+] THOMAS R. KNUTSON,[a] PAUL J. KUSHNER,[g] AMY R. LANGENHORST,[e,*] HYUN-CHUL LEE,[e,*] SHIAN-JIANN LIN,[a] JIAN LU,[d] SERGEY L. MALYSHEV,[h] P. C. D. MILLY,[f] V. RAMASWAMY,[a] JOELLEN RUSSELL,[c] M. DANIEL SCHWARZKOPF,[a] ELENA SHEVLIAKOVA,[h] JOSEPH J. SIRUTIS,[a] MICHAEL J. SPELMAN,[a] WILLIAM F. STERN,[a] MICHAEL WINTON,[a] ANDREW T. WITTENBERG,[a] BRUCE WYMAN,[a] FANRONG ZENG,[e] AND RONG ZHANG[c]

[a] *National Oceanic and Atmospheric Administration/Geophysical Fluid Dynamics Laboratory, Princeton University, Princeton, New Jersey*
[b] *Department of Environmental Sciences, Rutgers–The State University of New Jersey, New Brunswick, New Jersey*
[c] *Princeton University, Princeton, New Jersey*
[d] *UCAR Visiting Scientist Program, National Oceanic and Atmospheric Administration/Geophysical Fluid Dynamics Laboratory, Princeton, New Jersey*
[e] *RS Information Services, McLean, Virginia*
[f] *U.S. Geological Survey, and National Oceanic and Atmospheric Administration/Geophysical Fluid Dynamics Laboratory, Princeton, New Jersey*
[g] *Department of Physics, University of Toronto, Toronto, Ontario, Canada*
[h] *Department of Ecology and Evolutionary Biology, Princeton University, Princeton, New Jersey*

(Manuscript received 8 December 2004, in final form 18 March 2005)

ABSTRACT

The formulation and simulation characteristics of two new global coupled climate models developed at NOAA's Geophysical Fluid Dynamics Laboratory (GFDL) are described. The models were designed to simulate atmospheric and oceanic climate and variability from the diurnal time scale through multicentury climate change, given our computational constraints. In particular, an important goal was to use the same model for both experimental seasonal to interannual forecasting and the study of multicentury global climate change, and this goal has been achieved.

Two versions of the coupled model are described, called CM2.0 and CM2.1. The versions differ primarily in the dynamical core used in the atmospheric component, along with the cloud tuning and some details of the land and ocean components. For both coupled models, the resolution of the land and atmospheric components is 2° latitude × 2.5° longitude; the atmospheric model has 24 vertical levels. The ocean resolution is 1° in latitude and longitude, with meridional resolution equatorward of 30° becoming progressively finer, such that the meridional resolution is 1/3° at the equator. There are 50 vertical levels in the ocean, with 22 evenly spaced levels within the top 220 m. The ocean component has poles over North America and Eurasia to avoid polar filtering. Neither coupled model employs flux adjustments.

The control simulations have stable, realistic climates when integrated over multiple centuries. Both

* Current affiliation: National Oceanic and Atmospheric Administration/Geophysical Fluid Dynamics Laboratory, Princeton University, Princeton, New Jersey.
+ Current affiliation: Atmospheric Science Division L-103, Lawrence Livermore National Laboratory, Livermore, California.

Corresponding author address: Dr. Thomas L. Delworth, National Oceanic and Atmospheric Administration/Geophysical Fluid Dynamics Laboratory, P.O. Box 308, Princeton University, Princeton, NJ 08542.
E-mail: Tom.Delworth@noaa.gov

models have simulations of ENSO that are substantially improved relative to previous GFDL coupled models. The CM2.0 model has been further evaluated as an ENSO forecast model and has good skill (CM2.1 has not been evaluated as an ENSO forecast model). Generally reduced temperature and salinity biases exist in CM2.1 relative to CM2.0. These reductions are associated with 1) improved simulations of surface wind stress in CM2.1 and associated changes in oceanic gyre circulations; 2) changes in cloud tuning and the land model, both of which act to increase the net surface shortwave radiation in CM2.1, thereby reducing an overall cold bias present in CM2.0; and 3) a reduction of ocean lateral viscosity in the extratropics in CM2.1, which reduces sea ice biases in the North Atlantic.

Both models have been used to conduct a suite of climate change simulations for the 2007 Intergovernmental Panel on Climate Change (IPCC) assessment report and are able to simulate the main features of the observed warming of the twentieth century. The climate sensitivities of the CM2.0 and CM2.1 models are 2.9 and 3.4 K, respectively. These sensitivities are defined by coupling the atmospheric components of CM2.0 and CM2.1 to a slab ocean model and allowing the model to come into equilibrium with a doubling of atmospheric CO_2. The output from a suite of integrations conducted with these models is freely available online (see http://nomads.gfdl.noaa.gov/).

1. Introduction

This paper, along with its companion papers that follow in this issue, describes the formulation and simulation characteristics of two new global coupled climate models developed over the last several years at the Geophysical Fluid Dynamics Laboratory (GFDL) of the National Oceanic and Atmospheric Administration (NOAA). The models are the product of an effort to expand upon the capabilities of past models at GFDL that have been used to study issues of climate variability and change on seasonal to centennial time scales (see, e.g., Manabe et al. 1991; Hamilton et al. 1995; Rosati et al. 1997; Delworth et al. 2002). The goal of this effort has been to create models that can realistically simulate a range of phenomena from diurnal-scale fluctuations and synoptic-scale storms to multicentury climate change. An associated goal was to use the same model for experimental seasonal forecasting and the simulation of global climate change.

The coupled climate models are composed of separate atmosphere, ocean, sea ice, and land component models, which interact through a flux coupler module. The two coupled models described in this paper are called CM2.0 and CM2.1. The CM2.0 model uses atmospheric model (AM2.0) and land model (LM2.0) components that are nearly identical to those described in the 2004 paper by the GFDL Global Atmosphere Model Development Team [2004, hereafter referred to as GFDL_GAMDT; differences from the model described in GFDL_GAMDT are detailed in section 2a(2)]. The CM2.0 coupled model is run without flux adjustments and produces a realistic simulation of climate in many respects, as described in detail in sections 3, 4, and 5. However, this model experiences an equatorward drift of the midlatitude westerly winds and surface wind stress patterns after the atmosphere and oceans are coupled, contributing to a cold bias associated with an equatorward contraction of the oceanic subtropical gyre circulations.

The atmospheric component of CM2.0 uses a B grid dynamical core. When a version of the atmospheric model that uses a finite volume (FV) dynamical core (Lin 2004) is inserted in the CM2.0 coupled model, both the equatorward drift after coupling and the overall cold bias are substantially reduced. *Primarily because of the substantial improvement in the extratropical wind stress pattern and temperature biases, a second coupled model (CM2.1) was developed, using the FV atmospheric core.* In addition to using the FV dynamical core, the CM2.1 model incorporates several changes that were designed to reduce the model's overall cold bias (the details of the changes are reported in section 2). These consist of the following: 1) In the atmosphere, parameters in the cloud scheme were modified to increase the net shortwave radiation at the surface. 2) In the land model, evaporation was suppressed when the soil is frozen at a depth of 30 cm; this reduced late spring evaporation at higher latitudes of the Northern Hemisphere, thereby reducing cloudiness and increasing net surface shortwave radiation. 3) In the ocean component, a lower horizontal viscosity was used in the extratropics which strengthened the subpolar gyres. In the North Atlantic, the effect was to increase the polar heat transport of the subpolar gyre, thereby substantially reducing the cold bias and excessive sea ice seen there in CM2.0.

The difference in annual-mean zonal wind stress between the two versions of the coupled model (CM2.0 and CM2.1), and the contours of zero wind stress curl for the two models, are shown in Fig. 1. The positive values for the wind stress difference in the middle latitudes of each hemisphere reflect a more poleward location of the westerlies in this new version relative to CM2.0, which is of crucial importance for the simulated ocean circulation. This change in the latitude of the

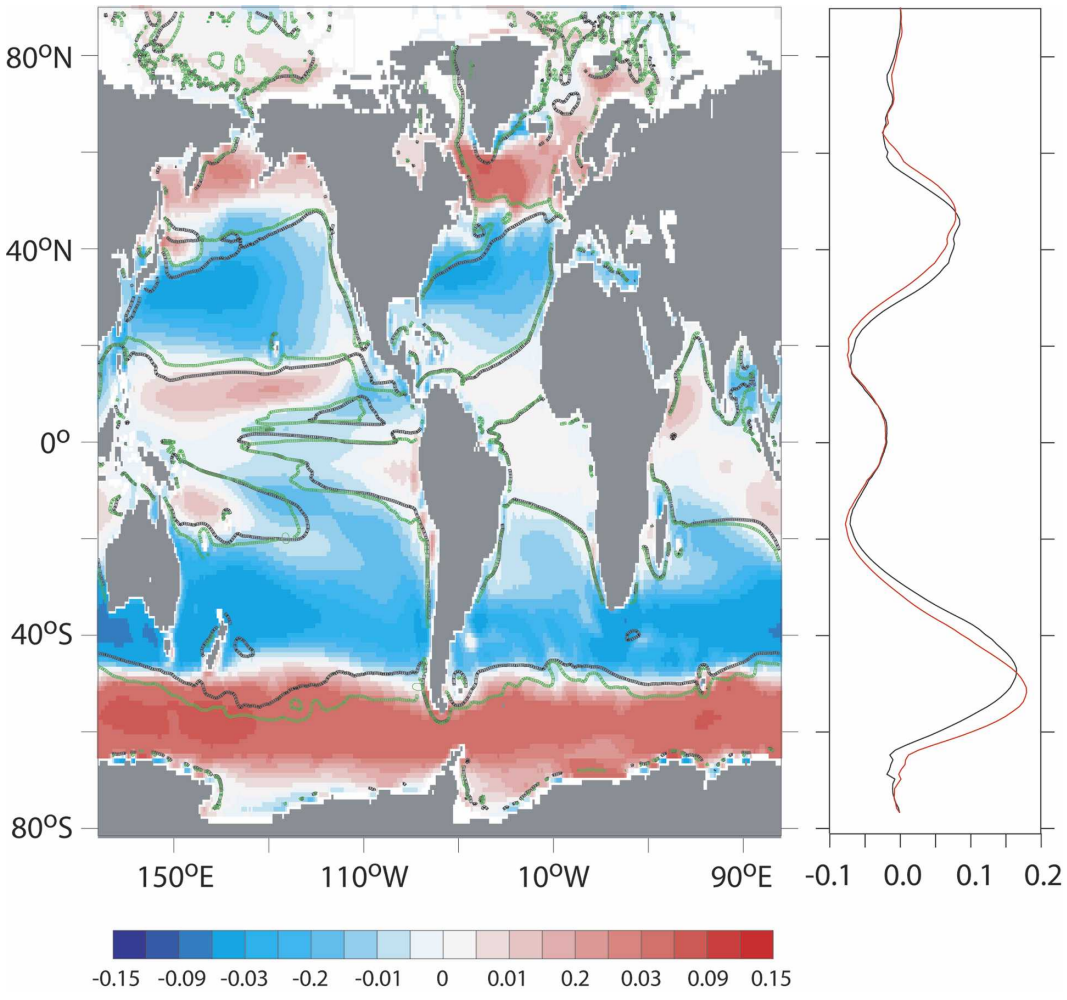

FIG. 1. (left) Color shading indicates the difference in annual-mean zonal wind stress, computed as the stress in CM2.1 minus the stress in CM2.0 for the 1990 control integrations (N m^{-2}). Positive values (red shading) denote increased westerly winds in CM2.1 relative to CM2.0. The solid black line indicates the zero wind stress curl line for CM2.0, and the green line indicates the zero wind stress curl line for CM2.1. The more poleward location of the zero wind stress curl line in CM2.1 is consistent with a poleward expansion of the oceanic gyre circulations. (right) Zonal means of the annual-mean zonal wind stress for CM2.0 (black) and CM2.1 (red). The more poleward location of the zonal wind stress in CM2.1 is clear.

westerlies is easily seen in the right panel of the figure, which shows the zonal means of the zonal wind stress. The zero wind stress curl line is also more poleward in CM2.1, in better agreement with observations, and of substantial importance for the oceanic gyre circulations. The reasons for the differing positions of the atmospheric winds are not well understood.

The time-mean errors in the simulation of sea surface temperature (SST) for the two coupled models (the details of the experimental design are described in section 2) are shown in Fig. 2. It is readily apparent that the errors in CM2.1 are substantially less than those in CM2.0. Quantitatively, the root-mean-square error (rmse) for SST in CM2.0 is 1.54 K, and it is 1.16 K for CM2.1. Most notable is the reduction of the cold bias in the North Pacific associated with a poleward expansion of the subtropical gyre. There is also a dramatic improvement in the simulation of the Southern Ocean in CM2.1 relative to CM2.0 (Gnanadesikan et al. 2006, hereafter Part II).

As described in detail in the following sections, although many features are improved in CM2.1 relative to CM2.0, some are not. For example, although the overall temperature bias in CM2.1 is much lower than in CM2.0, the simulation of precipitation is somewhat worse in CM2.1 than CM2.0. This is certainly typical in the development of such models, in that many features can change in response to changes in the model formu-

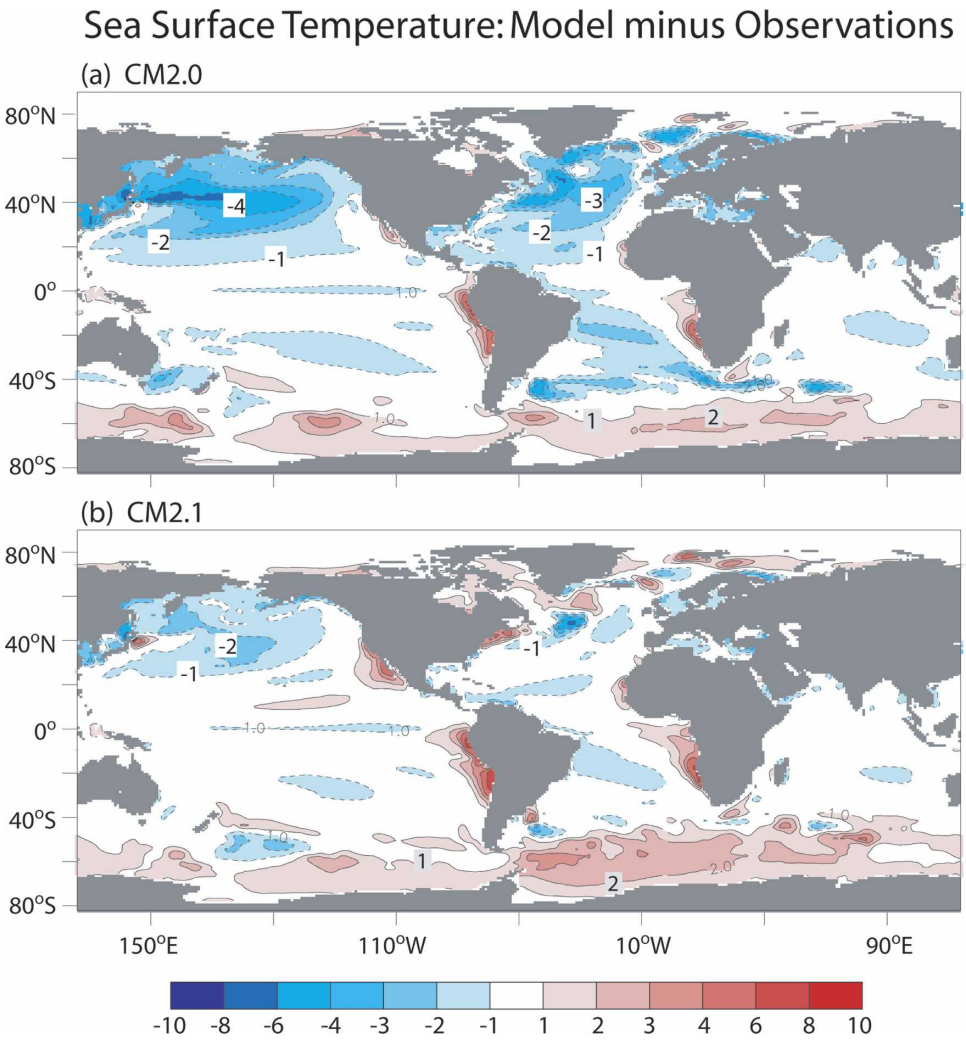

FIG. 2. Maps of errors in simulation of annual-mean SST (K). The errors are computed as model minus observations, where the observations are from the Reynolds SST data [provided by the National Oceanic and Atmospheric Administration–Cooperative Institute for Research in Environmental Sciences (NOAA–CIRES) Climate Diagnostics Center, Boulder, CO, from their Web site at http://www.cdc.noaa.gov/]. (a) CM2.0 (using model years 101–200). (b) CM2.1 (using model years 101–200). Contour interval is 1 K, except that there is no shading for values between –1 and +1 K.

lation, and those changes have both benefits and drawbacks in terms of the fidelity of the simulation.

Both models have been used to run a suite of climate change experiments for the 2007 Intergovernmental Panel on Climate Change (IPCC) Assessment Report 4 (AR4) and are able to simulate the main features of the observed warming of the twentieth century (Knutson et al. 2006). Output from these model simulations is freely available online (see http://nomads.gfdl.noaa.gov/). The climate sensitivity associated with each model has been evaluated. To evaluate climate sensitivity, the atmosphere, land, and sea ice components of either CM2.0 or CM2.1 are coupled to a slab mixed layer ocean. The climate sensitivity is then defined as the equilibrium response of global-mean surface air temperature in the slab ocean coupled model to a doubling of atmospheric CO_2. Thus defined, the climate sensitivity associated with CM2.0 is 2.9 K, and for CM2.1 it is 3.4 K. Additional investigations are underway to assess why the climate sensitivities differ.

This paper is the first of four that describe the coupled models. This paper describes the coupled model formulation, drifts in the solutions after coupling of the component models, and aspects of the time-mean solution, with emphasis on the oceanic surface and atmosphere. The following paper (Part II) describes in more detail the formulation of the ocean component of the coupled models and the time-mean properties of

the ocean in coupled model simulations. The next paper in this set (Wittenberg et al. 2006, hereafter Part III) provides an in-depth analysis of ENSO as simulated in the models, including its extratropical teleconnections. Finally, Stouffer et al. (2006, hereafter Part IV) describes the response of the models to idealized radiative forcing changes. Additional details on the formulation of the ocean model, with emphasis on the numerics and physical parameterizations, are in Griffies et al. (2005).

Detailed analyses of other aspects of these models, including their response to estimates of the changing radiative forcing from 1861 to 2000, will be reported in future papers.

2. Model formulation

The coupled model consists of four component models: atmosphere, land, sea ice, and ocean. A coupler computes and passes fluxes between the component models and does all the necessary regridding so that each component receives inputs and supplies outputs on its own grid. All fluxes are conserved to within machine precision. There are no flux adjustments[1] used in these models.

a. Atmosphere and land models

1) OVERVIEW

The atmosphere and land components of coupled model CM2.0 are referred to as AM2.0 and LM2.0, respectively, and are documented in GFDL_GAMDT,[2] with a few modifications as noted below. The atmosphere and land horizontal resolution is 2° latitude × 2.5° longitude; the atmospheric model has 24 levels in the vertical. The model uses a 3-h time step for atmospheric radiation and a 0.5-h time step for other atmospheric physics, and includes a diurnal cycle of insolation. The land model employed is the Land Dynamics model (LaD; Milly and Shmakin 2002) and includes a river routing scheme that moves runoff collected over the model's drainage basins to river mouths, where the freshwater is injected into the model ocean.

[1] Flux adjustments may be used in coupled models to help maintain a realistic time-mean state. The flux adjustments are calculated prior to the start of a coupled model integration and are constant additive terms to the surface fluxes, usually for the heat and freshwater fluxes.

[2] In other contexts, in which our internal model development is described in more detail, the model in GFDL_GAMDT is referred to as AM2p12b, and AM2.0 (the atmospheric component of CM2.0) is referred to as AM2p13.

TABLE 1. Model input parameters related to radiative forcing for the 1860 and 1990 control integrations.

	1860	1990
Solar irradiance	1364.67 W m^{-2}	1366.86 W m^{-2}
CO_2	285.98 ppmv[a]	352.72 ppmv
CH_4	804.9 ppbv[b]	1688.625 ppbv
F11	0 pptv[c]	259 pptv
F12	0 pptv	466.375 pptv
F22	0 pptv	89.25 pptv
F113	0 pptv	71.375 pptv
N_2O	275 ppbv	308.45 ppbv
Land cover	1860 distribution	1990 distribution

[a] Parts per million by volume.
[b] Parts per billion by volume.
[c] Parts per trillion by volume.

2) DIFFERENCES OF AM2.0/LM2.0 FROM THE ATMOSPHERE/LAND MODEL DESCRIBED IN GFDL_GAMDT

The differences between AM2.0/LM2.0 and the atmosphere and land models described in GFDL_GAMDT are relatively minor. First, in an attempt to address a persistent cold bias, the net surface shortwave radiation in the model was increased. This was accomplished through a 45% increase (from 4.7×10^{-6} s^{-1} to 6.8×10^{-6} s^{-1}) in the cloud scheme parameter that controls the rate of erosion of clouds under convective conditions.

Second, the Caspian Sea is now treated as a special land surface type. This is necessary since the Caspian Sea is not included as part of the ocean model, and there is no lake model within LM2.0. The Caspian Sea is maintained as a saturated surface; if the predicted soil water for any grid box in the Caspian Sea exceeds saturation, the excess water is treated as runoff and is routed to the ocean point corresponding to the mouth of the Indus River. Conversely, if the predicted soil water at any grid point in the Caspian Sea is less than saturation, sufficient freshwater is moved instantaneously from the ocean at the mouth of the Indus river to the Caspian Sea to maintain saturation. Thus, the atmospheric model sees the Caspian Sea as a saturated surface, while global water conservation is maintained.

Third, a revised set of 1990 radiative conditions was employed, which includes updated specifications for well-mixed greenhouse gases, tropospheric and stratospheric ozone, the three-dimensional distribution of natural and anthropogenic aerosols, solar irradiance, and the distribution of land cover types. Values for the well-mixed greenhouse gases and solar irradiance are listed in Table 1. The specified anthropogenic aerosols include black carbon, organic carbon, and sulfate aerosols. Natural aerosols include sea salt and dust. The

three-dimensional distributions of monthly mean aerosols are specified based on output from the Model for Ozone and Related Chemical Tracers (MOZART) chemical transport model (Horowitz et al. 2003), which uses input emissions from Olivier et al. (1996) and Cooke et al. (1999). Stratospheric ozone distributions were prescribed based on Randel and Wu (1999). Volcanic aerosols are assumed to be zero in the control integrations described below. The aerosol optical properties follow Haywood et al. (1999). Note that the aerosols do not directly interact with the cloud scheme so that any indirect effects are omitted in CM2.0 and CM2.1.

Dust concentrations were from multiyear simulations driven by the National Centers for Environmental Prediction (NCEP)–National Center for Atmospheric Research (NCAR) reanalysis (Kalnay et al. 1996). Vegetation-free surfaces are regarded as dust sources following Ginoux et al. (2001). The dust size distribution is discretized into eight bins ranging in size from 0.1 to 10 microns. For sea salt, a constant concentration is assigned throughout the well-mixed marine boundary layer (up to 850 mb), and a zero concentration is prescribed above 850 mb and over land (Haywood et al. 1999).

The CM2 land-cover-type distribution is a combination of a potential natural vegetation-type distribution and a historical land use distribution dataset. The potential natural vegetation classification is based on that used in LaD (Milly and Shmakin 2002). The classification has 10 vegetation or land surface types (broadleaf evergreen, broadleaf deciduous, mixed forest, needleleaf deciduous, needle-leaf evergreen, grassland, desert, tundra, agriculture, and glacial ice). As described in section 2f, experiments were performed with land cover distributions representative of either 1860 or 1990 conditions, which were derived from available land use change data.

3) Differences between atmosphere/land components of CM2.0 and CM2.1

The atmosphere and land components of coupled model CM2.1 are referred to as AM2.1 and LM2.1, and have approximately the same spatial resolution as AM2.0/LM2.0 (although the precise grid is slightly different, as the atmospheric dynamics are done using both a C and D grid in AM2.1, versus a B grid in AM2.0). AM2.1/LM2.1 differs from AM2.0/LM2.0 in several ways. First, the dynamical core of AM2.1 uses FV numerics (Lin 2004). This difference alone accounts for changes in the surface wind stress pattern that lessen the drift after coupling. Second, a tuning of the cloud scheme was necessary when using the FV core to achieve an approximate radiative balance; further tuning produced a small positive net radiative imbalance when using SSTs from the recent past. The two specific cloud tuning changes, both of which act to increase the net shortwave radiation at the surface, were that (i) the value of the cloud drop radius threshold value for the onset of raindrop formation was reduced from 10.6 μm in AM2.0 to 8 μm in AM2.1, and (ii) the parameter controlling the rate of erosion of clouds under convective conditions was increased by 18% (from 6.8×10^{-6} s^{-1} in AM2.0 to 8×10^{-6} s^{-1} in AM2.1). Third, the land model was modified to suppress evaporation from land when soil is frozen at a depth of about 30 cm. This has a significant warming impact by reducing evaporation, and hence cloudiness, at higher latitudes of the Northern Hemisphere during late spring and summer, resulting in enhanced shortwave radiation at the surface and warmer near-surface air temperature. However, this change also contributes to a thinning of the Arctic sea ice, which amplifies an existing bias toward thin Arctic sea ice (described below). Fourth, the Amur River (far eastern Asia) drains into the Sea of Japan in CM2.1 instead of the Sea of Ohkotsk as in CM2.0 (in reality it drains into a strait connecting the two seas). This has a relatively minor impact. When run using observed SSTs over the period 1982–98, the AM2.1 model has a net radiative imbalance at the top of the atmosphere of 0.25 W m^{-2}. This integration includes observational estimates of well-mixed greenhouse gases, anthropogenic aerosols, volcanic aerosols, solar irradiance changes, and land use changes.

b. Ocean model

The ocean model formulation and physical parameterizations are described in detail in Part II and Griffies et al. (2005) and are based on the Modular Ocean Model code (MOM4; Griffies et al. 2003). The ocean component for CM2.0 is referred to as OM3.0, and the ocean component for CM2.1 is referred to as OM3.1. The ocean model resolution (for both OM3.0 and OM3.1) is 1° in latitude and longitude, with meridional resolution equatorward of 30° becoming progressively finer, such that the meridional resolution is 1/3° at the equator. There are 50 vertical levels in the ocean, with 22 levels of 10-m thickness each in the top 220 m. A tripolar grid with poles over Eurasia, North America, and Antarctica is used to avoid polar filtering over the Arctic (Murray 1996).

The model uses a true freshwater flux boundary condition (not a virtual salt flux, which has been used in previous coupled models). River flow into the ocean is predicted and is based upon a predetermined river drainage map determined from available global river

networks and topographic maps. Any runoff from land cells is routed to an ocean discharge point, with a delay that varies from basin to basin. The water is injected into the ocean evenly over the top 40 m (four levels) of the ocean. Because the model uses a true freshwater flux, this river flow adds mass to the ocean. There are six inland seas (Hudson Bay, Black Sea, Mediterranean Sea, Red Sea, Baltic Sea, and the Persian Gulf) that are connected to the World Ocean only via mixing processes at the connecting points between the inland seas and the open ocean.

The primary differences between OM3.0 and OM3.1 are in the parameter settings for some of the subgrid-scale physics, and the time-stepping algorithm. Poleward of 30° latitude, OM3.1 has a factor of 5 smaller horizontal viscosity, leading to more vigorous subpolar gyre circulations. The OM3.1 two-level time-stepping algorithm permits a 2-h ocean time step to be used, versus a 1-h time step in the three-level leapfrog scheme of OM3.0. Solutions using the two time-stepping schemes are virtually identical.

c. Sea ice model

The sea ice component of CM2.0 and CM2.1 is the GFDL Sea Ice Simulator (SIS). SIS is a dynamical model with three vertical layers, one snow and two ice, and five ice thickness categories. The elastic–viscous–plastic technique (Hunke and Dukowicz 1997) is used to calculate ice internal stresses, and the thermodynamics is a modified Semtner three-layer scheme (Winton 2000). Details of the model formulation and configuration are given in the appendix. The same sea ice model is used in CM2.0 and CM2.1.

d. Coupling

GFDL's CM2 models make use of the Flexible Modeling System (FMS; http://www.gfdl.noaa.gov/~fms/) coupler for calculating and passing fluxes between its atmosphere, land, sea ice, and ocean components. The atmosphere, ocean, land and sea ice exchange fluxes every hour in CM2.0, and every 2 h in CM2.1 (corresponding to the ocean time step for each model). Most surface fluxes are calculated on the *exchange grid* between two component grids using component properties that have been placed on this grid. The exchange grid is the set of polygons formed from the union of the cell boundaries of the two component grids. This procedure ensures that fluxes are calculated at the finest scale before averaging onto the coarser component grids. All fluxes are perfectly conserved to within machine precision. Land grid cells, which are otherwise identical in horizontal extent to atmospheric cells, are reduced in area at the coast by the areas of overlapping ocean cells so that the land and ocean perfectly tile the globe. Some properties from the coarser atmosphere model are placed onto the exchange grid using a second-order accurate technique (Jones 1999) to avoid noisy fluxes on the oceanic side.

e. 1860 and 1990 control integrations

Two types of control integrations are conducted, differing in the atmospheric trace gas and aerosol concentrations, insolation, and distribution of land cover types. For each control integration, aerosol and trace gas concentrations, insolation, and distribution of land cover types do not vary from one year to the next. In the so-called 1990 (1860) control integrations, these values are taken to represent 1990 (1860) values. The specific values used for well-mixed greenhouse gases and solar irradiance are listed in Table 1. Three-dimensional distributions of natural aerosols from sea salt and dust are also prescribed and are identical in the 1860 and 1990 control runs. The three-dimensional distributions of anthropogenic aerosols are prescribed and differ between 1860 and 1990 conditions (anthropogenic aerosols are assumed to be zero in the 1860 control integration). For the control integrations described here, there are no aerosols from volcanic sources.

When we compare the model simulations to observations, we focus on the 1990 control integrations, because this radiative forcing might be expected to yield a simulation closer to current observations. However, because there is a positive net radiative imbalance in the 1990 control integrations (discussed below), there are long-term drifts in simulations using the 1990s forcings, making them less desirable as control simulations for climate change experiments. Therefore, the climate change simulations described in Part IV are conducted as departures from the 1860 control integrations, which have much smaller net radiative imbalances, and therefore much smaller climate drifts. The 1860 control integrations are longer in duration than the 1990 control integration. A few of the differences in simulation characteristics between the 1860 and 1990 control integrations are presented in section 3. The 1990 control integrations are 300 yr in length for both models. The 1860 control integration for CM2.0 is 500 yr in length; for CM2.1 the 1860 control integration has run for more than 1000 yr.

f. Initialization

Different procedures were used to initialize the 1860 and 1990 control integrations. For the 1990 control integrations, the atmospheric and land initial conditions are taken from the end of a 17-yr run of the atmosphere–land model that uses observed time-varying

SSTs and sea ice over the period 1982–98. To derive the ocean initial conditions, a 1-yr integration of the ocean component of the coupled model is conducted starting from observed climatological conditions [taken from Steele et al. (2001), which is an extension of Antonov et al. (1998) and Boyer et al. (1998)], with the ocean initially at rest. The ocean model is forced with heat and water fluxes from an integration of the atmosphere model described above, along with observed wind stress; in addition, surface temperature and salinity are restored to the Steele et al. (2001) climatology with a 10-day restoring time scale. The purpose of the 1-yr run is to avoid initializing the coupled model with an ocean at rest. Output from the end of that one year spin up is taken as the initial condition for the coupled run. The sea ice initial conditions are taken from the end of year 10 of a preliminary coupled integration with the same model.

To derive initial conditions for the 1860 control integration, the method outlined in Stouffer et al. (2004) was used. Starting from a point in the first few decades of the 1990 control integration, the radiative-forcing conditions are changed from 1990 to 1860 values. With these 1860 radiative forcings, a multicentury spinup phase is conducted, thereby allowing the simulated climate system to adjust to these new forcings. These adjustment periods (300 yr were used for CM2.0, and 220 yr for CM2.1) are discarded, and are not part of the analyses shown below. Thus, what is labeled as year 1 of the CM2.0 (CM2.1) 1860 control integration corresponds to a time 300 (220) yr after the 1860 radiative forcings are introduced, thus allowing the system to adjust (at least partially) to the new radiative forcing.

3. Model stability and drift

After coupling the component models and starting from the set of initial conditions, the climate system is typically not in equilibrium, and undergoes a drift toward a more equilibrated state. The time series of global-mean SST for the two 1990 control experiments are plotted in Fig. 3a (the time series of global-mean surface air temperature look very similar). Both models experience drift for some considerable period after coupling, with an initial rapid cooling in SST, followed by a slow warming trend. As will be shown below, this latter feature is related to a persistent positive radiative imbalance. It is apparent that the overall state of CM2.1 is significantly warmer at the sea surface. The drift in SST for the 1860 control integrations (Fig. 3b) is smaller, consistent with the state being closer to radiative equilibrium as discussed below. Time series of global-mean surface air temperature (not shown) have a very similar behavior.

Another measure of drift is the top-of-the-atmosphere (TOA) net radiative imbalance (downward shortwave – upward shortwave – outgoing longwave), shown in Fig. 3c. There is a persistent positive imbalance in the 1990 control integrations of 0.5–2.0 W m^{-2}, indicating a net long-term gain of heat by the system. For this model, the net imbalance at the TOA is larger than the actual heat gain by the climate system, for at least three reasons. First, the AM2.0/LM2.0 model does not perfectly conserve heat and loses heat at a rate of approximately 0.3 W m^{-2}. This loss is quite uniform in time, and we do not expect it to be a significant issue in climate change experiments. This loss is smaller in AM2.1/LM2.1. Second, in both models there is a heat sink associated with glaciers; a heat balance is computed in the model over glacial surfaces, such that if the surface temperature of a glacial surface is computed to be above the freezing point, the temperature is reset to freezing, and the heat associated with this temperature change is lost from the system (estimated at approximately 0.05 W m^{-2}). Third, there is a heat sink in the ocean; when a mass of water is added to the ocean (via precipitation or river flow), the water mass assumes the temperature of the sea surface. In general, there is a net addition of water to the ocean at higher latitudes where it is cold, and a net removal of water from the ocean at lower latitudes where it is warm. The ocean must supply the heat necessary to warm this mass of water as it moves from colder to warmer regions. This heat is lost from the system when the water evaporates because condensate in the atmospheric model has no heat capacity. This loss is estimated at 0.17 (0.14) W m^{-2} in the 1990 control integrations of CM2.0 (CM2.1). (This term is estimated as the areal average over the global ocean of the product of the surface water flux and SST, multiplied by the density of water and the heat capacity of water. Calculations were performed using monthly data over years 281–300 of the 1990 control integrations.) This sink arises in this model because it uses a true freshwater flux from the atmosphere to the ocean. This topic needs to be addressed in future model development efforts.

A different representation of the heat imbalance of the model climate system is shown in Fig. 3e, which shows the rate of change of ocean heat content expressed as a net heating in W m^{-2}. Ocean heat content is the dominant mechanism of heat storage in the global climate system. The values shown in Fig. 3e are smaller than the TOA values for the reasons stated above and gradually decrease over time as the system approaches a more equilibrated state.

Note that the corresponding time series for the 1860 control integrations (Figs. 3d,f) show smaller imbal-

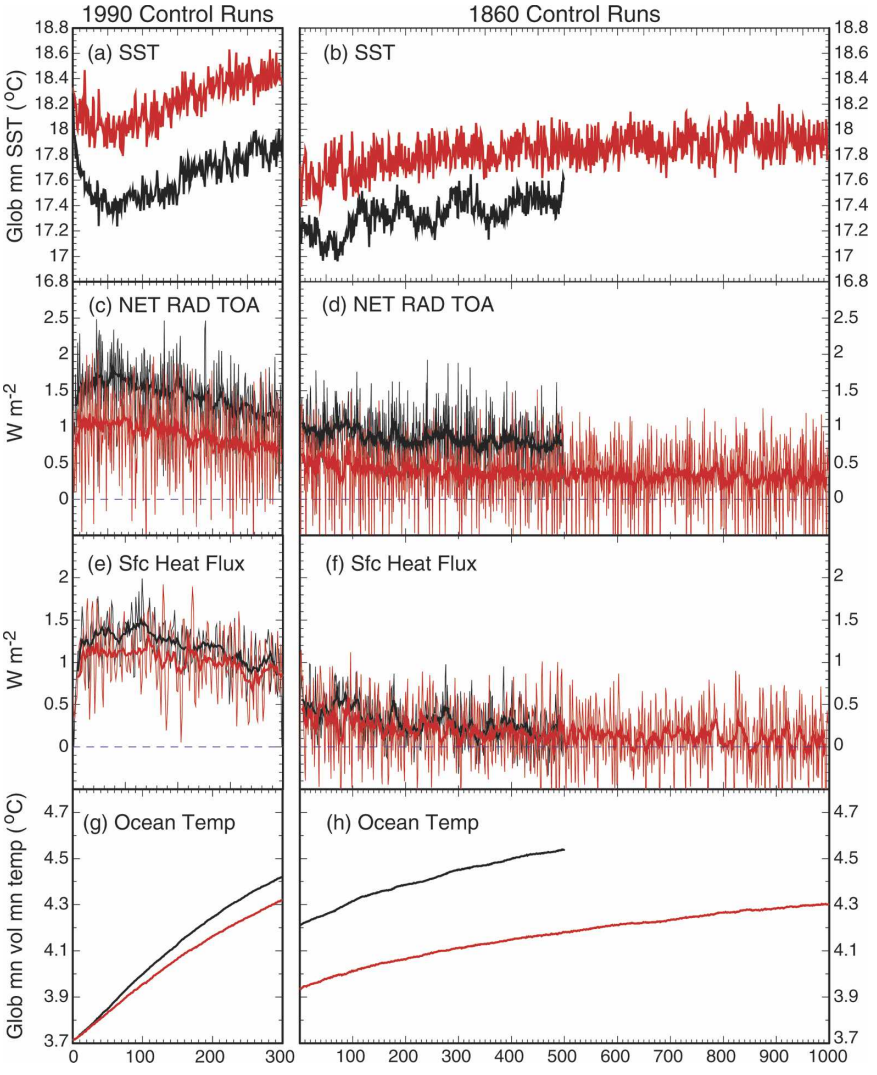

FIG. 3. Time series of annual-mean, global-mean quantities for the 1990 and 1860 control runs of CM2.0 (black lines) and CM2.1 (red lines). (left) The 1990 control runs, and (right) the 1860 control runs. (a), (b) SST and (c), (d) TOA net radiative imbalance; thin lines are annual-mean values, and thick lines are 11-yr running means. (e), (f) Surface heat flux into the ocean, calculated as the temporal derivative of the global ocean heat content, expressed as W m^{-2}; thin lines are annual means, and thick lines are 11-yr running means. (g), (h) Volume-mean temperature for the full-depth global ocean.

ances. In general, the 1860 simulations are much closer to radiative equilibrium than the 1990 control integrations.

The heat imbalances described above are directly related to the time series of volume-mean ocean temperature averaged over the globe. These are shown in Fig. 3g and Fig. 3h. There are significant subsurface drifts throughout the multiple centuries of the integrations, reflecting the heat stored in the ocean, and it will take many centuries for the full-depth ocean to come into equilibrium (Stouffer 2004). The drifts in volume-mean ocean temperature are considerably smaller in the 1860 control integration. The smaller drifts in the 1860 control integrations make them much more suitable as control integrations for climate change simulations.

The vertical distribution of the temperature bias of the global ocean is shown in Fig. 4 for the 1990 control integrations. In both models the near-surface ocean initially cools, after which there is a gradual surface warming. The deeper ocean layers clearly evolve on a much longer time scale. The vertically averaged warming (as in Fig. 3) is reflective of the net positive heat imbalance for the 1990 control integration. In addition to the vertically averaged warming, there is also a vertical redistribution of heat, with a tendency for cooling in the

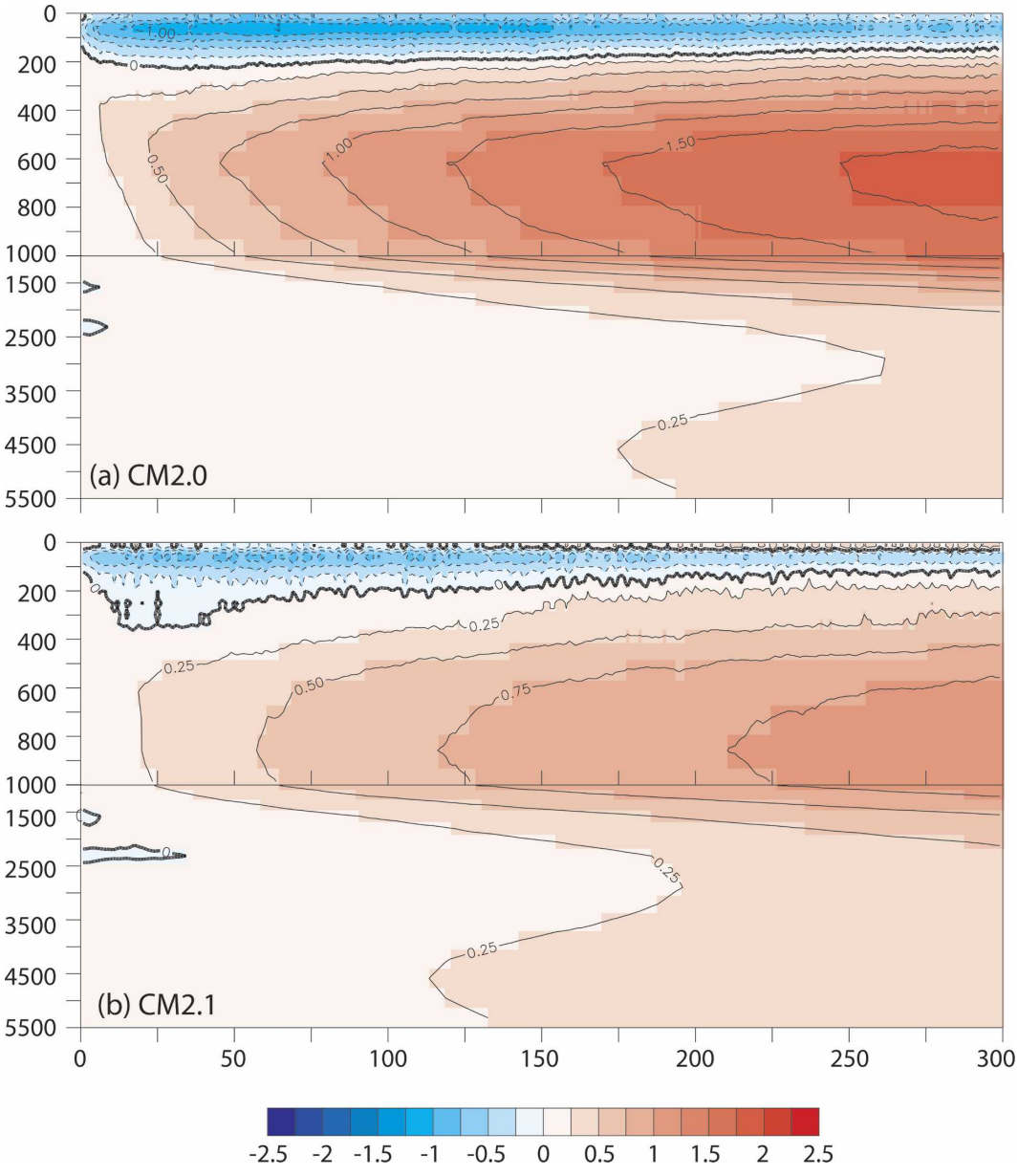

FIG. 4. Differences between simulated and observed global-mean ocean temperature (K) as a function of depth and time. For each year, the difference is computed as the global-mean simulated temperature minus the long-term observed mean temperature. (a) CM2.0 1990 control integration. (b) CM2.1 1990 control integration.

upper ocean and subsurface warming. The subsurface warming is smaller in CM2.1 than CM2.0. One contributing factor for this difference is the change in the wind stress pattern noted previously in CM2.1, with associated changes in the location and character of subduction zones associated with the ocean subtropical gyre circulations. A more poleward location of the subduction zones implies that relatively colder water is subducted, and thus less heat is supplied to the ocean interior. Consistent with the smaller radiative imbalance, the rate of subsurface warming in the 1860 control integrations is smaller (not shown).

The spatial patterns of the subsurface warming in the 1990 control integrations are plotted in Fig. 5. Temperature departures from observations at 700-m depth are evident in both models. The warming is largely associated with the subtropical gyre circulations, especially in the Northern Hemisphere. A notable difference between CM2.0 and CM2.1 appears in the South Pacific; the positive temperature anomalies in CM2.0

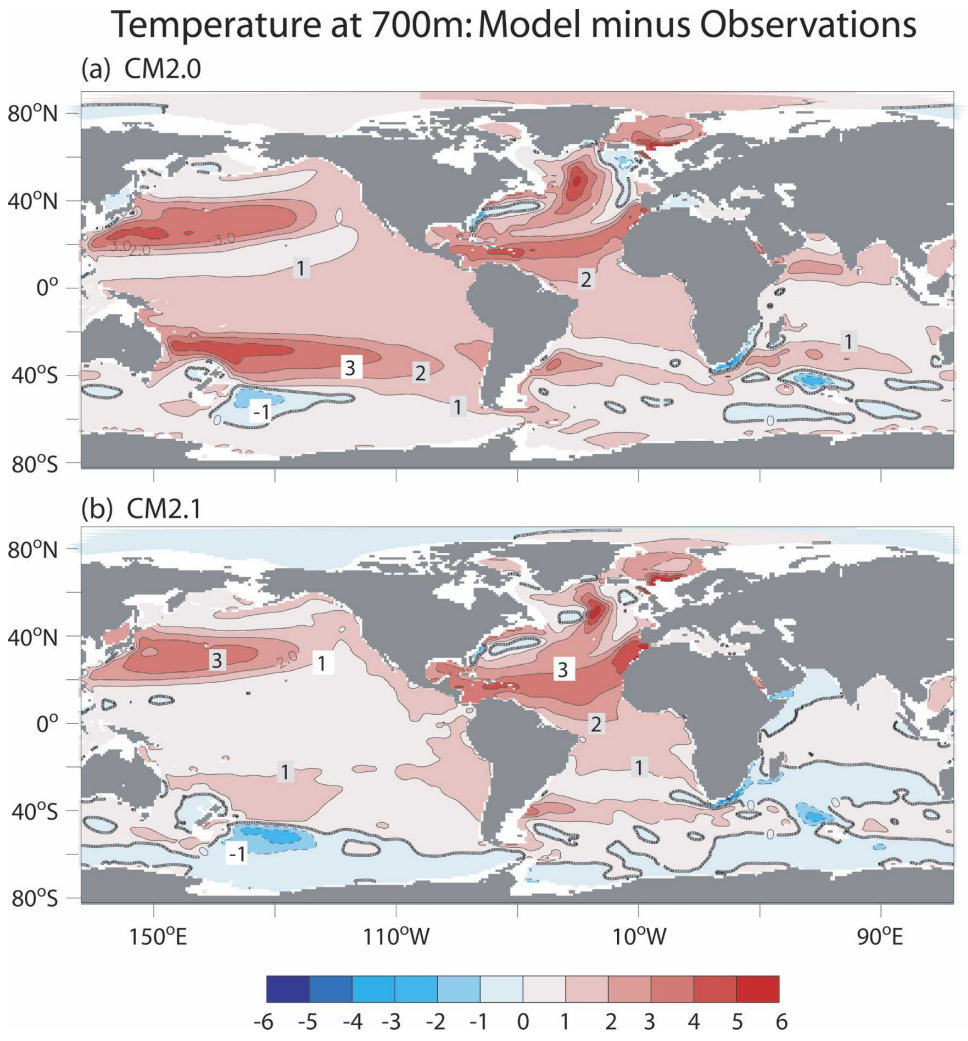

FIG. 5. Simulated − observed ocean temperature (K) at 700-m depth for 1990 control integrations. (a) CM2.0 (years 101–200) and (b) CM2.1 (years 101–200).

are virtually absent in CM2.1. Separate analyses suggest that this is a consequence of the more poleward location of the westerly atmospheric winds in CM2.1 relative to CM2.0. It should be noted that the global-mean of the large subsurface warming shown here is associated with the sustained positive radiative imbalance in the 1990 control integration; such warming is much smaller in the 1860 control integrations (not shown) and is associated with their smaller radiative imbalances.

The evolution of global sea surface salinity (SSS) is shown in Fig. 6. In the initial stages of the 1990 control integrations, the models have a tendency to drift toward fresher conditions in the surface layers. This freshening tendency, especially in the North Atlantic, has been an ongoing focus of our model development efforts and is substantially improved in CM2.1. Several factors have contributed to this improvement. An improved simulation of surface wind stress is important, particularly through the poleward expansion of the oceanic subtropical gyres and associated salinity distribution. The reduced ocean-horizontal viscosity in CM2.1 is important in reducing SSS biases regionally in the North Atlantic by increasing the strength of the subpolar gyre circulation and associated salt transports. There is virtually no drift in global-mean SSS for both 1860 control integrations.

The time–depth evolution of the global salinity bias is shown in Fig. 7. The fresh drift in the upper several hundred meters is evident and is compensated for by weaker increases in salinity in the larger volume of the deep ocean. The fresh and salty drifts are considerably reduced in CM2.1.

The evolution of the models' North Atlantic thermo-

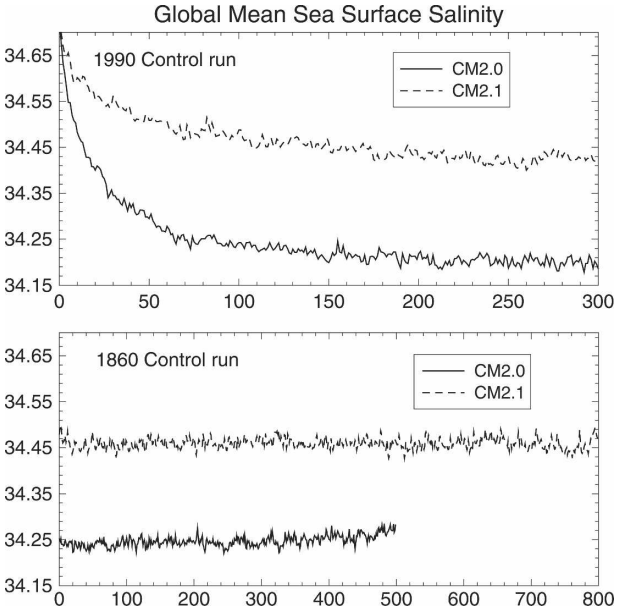

FIG. 6. Time series of annual-mean, global-mean SSS (psu). Time series for the (top) 1990 and (bottom) 1860 control integrations of models CM2.0 and CM2.1.

haline circulation (THC) is shown in Fig. 8 for both the 1990 and 1860 control integrations. Talley et al. (2003) provides a recent observational estimate of 18 Sv (1 Sv $\equiv 10^6$ m^3 s^{-1}). After some adjustments in the first few decades of the 1990 control integrations, both models have attained a stable THC value, with unforced decadal and multidecadal-scale fluctuations. The higher average THC value in CM2.1 is associated with both a lower value of ocean viscosity in CM2.1, as well as the altered wind stress pattern in CM2.1. In a separate test (not shown) of two experiments in which only the viscosity differs, the THC is 3.2 Sv stronger in the lower viscosity experiment over the last 80 yr of the 100-yr experiments. One of the effects of the lower viscosity is to enhance the strength of the oceanic subpolar gyre circulation in the North Atlantic, thereby increasing the flow of warm, saline waters into the Labrador and Greenland Seas, enhancing the formation of deep water. This also increases the poleward transport of saline near-surface waters in the North Atlantic. The decrease in the THC over the first few decades in the CM2.0 1990 control integration (black line in Fig. 8) is related to an increasing near-surface fresh bias in the North Atlantic. The stability of the THC is evident in the 1860 control integrations, with no trends in the THC. Both models show a tendency for distinct interdecadal fluctuations of the THC, which will be the subject of a future study.

The models' Antarctic Circumpolar Current (ACC) transport is shown in Fig. 9 for both the 1990 and 1860 control integrations. Cunningham et al. (2003) provides an observational estimate of the strength of the ACC as 134 Sv, but there is considerable uncertainty in this number. In the 1990 control integration for both models there is an adjustment of the ACC over the first century, after which values stabilize. There is a significant difference between the two models, consistent with the differences in simulated zonal wind stress shown in Fig. 1. The more poleward maximum in westerly winds translates to a strengthened ACC in CM2.1 relative to CM2.0. The lower viscosity in CM2.1 also contributes to a stronger ACC. Centennial-scale fluctuations of the ACC are apparent, particularly in the 1860 control run of CM2.0. The mechanism of these fluctuations has not been analyzed in detail but appears to be related to centennial-scale fluctuations in convection and vertically averaged ocean temperature.

The time series of annual-mean sea ice extent are shown in Fig. 10. For the Northern Hemisphere, CM2.0 has a tendency for excessive sea ice extent early in the 1990 integration, but this tendency diminishes over time, consistent with the slow warming trend in global SST shown in Fig. 3a. The Northern Hemisphere sea ice extent in CM2.1 is similar to observed, although there are significant seasonal errors (also for CM2.0), with excessive extent in the winter and insufficient extent in the summer (as shown later in Fig. 14). For the Southern Hemisphere, both models have insufficient sea ice, related to excessive shortwave radiation incident at the surface (discussed below).

4. Time-mean simulation characteristics

The time-mean simulation characteristics of the 1990 control integrations from the two coupled models are presented in this section. We focus on oceanic surface and atmospheric fields. The three-dimensional structure of the ocean simulation is discussed in detail in Part II.

a. Ocean heat transport

The meridional transport of heat by the oceans is an important factor in the ability of models to simulate realistic climate. The total simulated meridional transports of heat by the ocean, as well as an observational estimate, are shown in Fig. 11. For the entire globe, the northward transport in the NH poleward of 10°N is consistent with observational estimates, but there appears to be insufficient southward transport of heat out of the Tropics in the models. This discrepancy is most apparent in the Indo-Pacific sector (bottom panel). The

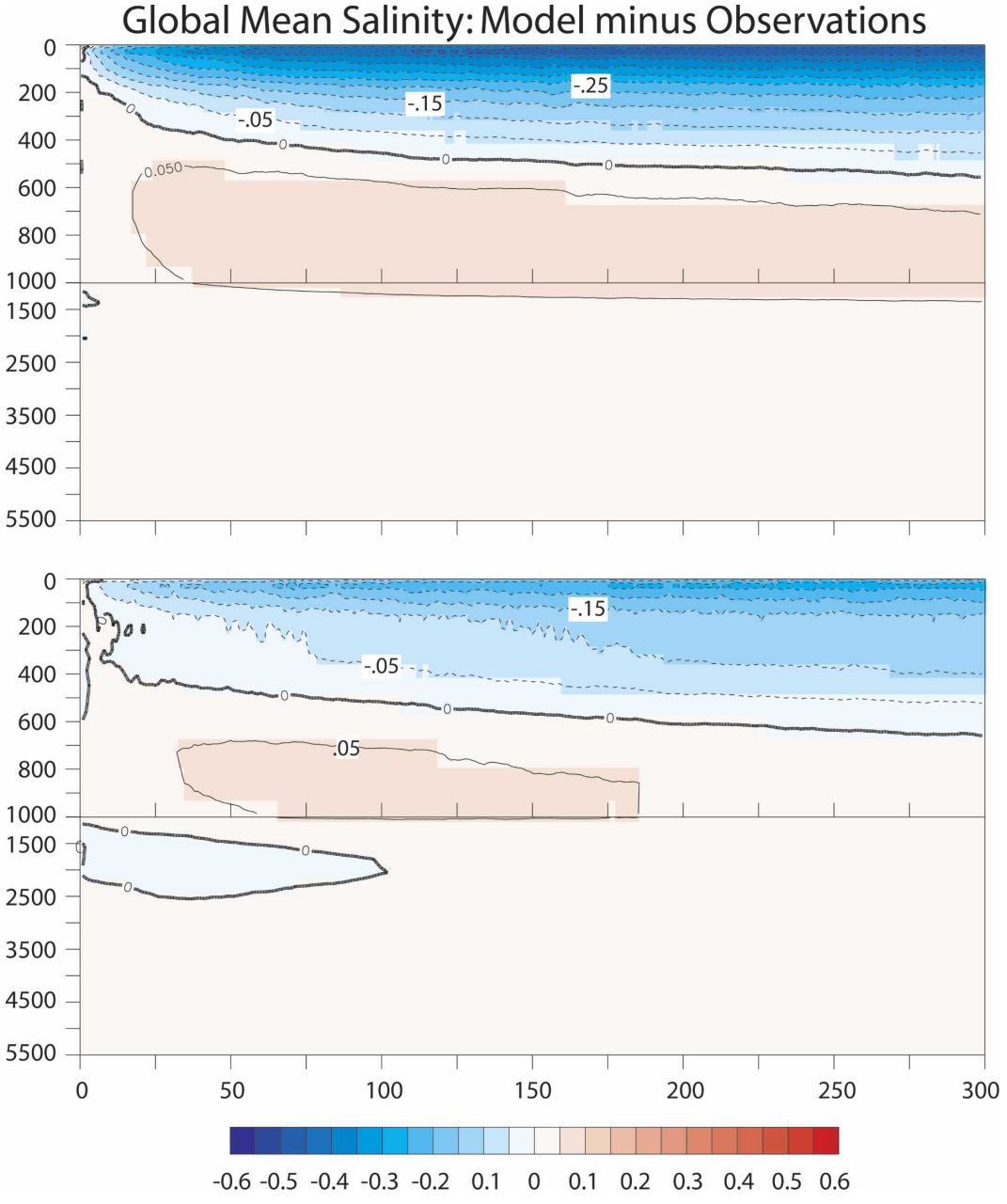

FIG. 7. Annual-mean, global-mean salinity (psu) error as a function of depth and time. For each year, the difference is computed as the global-mean simulated salinity minus the long-term observed mean salinity: (a) CM2.0 and (b) CM2.1.

heat transport in the Atlantic is in good agreement with observational estimates, with just over 1 PW maximum northward heat transport around 20°N. Significant uncertainties exist in the observational estimates of ocean heat transport.

b. Ocean surface

The spatial patterns of the errors in simulation of annual-mean sea surface temperature were shown in Fig. 2 for CM2.0 (years 101–200) and CM2.1 (years 101–200). Both models show a tendency for positive SST errors in the high latitudes of the Southern Hemisphere. This is consistent with a known characteristic of both AM2.0/LM2.0 and AM2.1/LM2.1, in which excessive shortwave radiation is incident upon the sea surface (see Fig. 10 of GFDL_GAMDT, as well as Fig. 15 of this paper). Both models have a tendency for negative errors in the extratropics of the Northern Hemi-

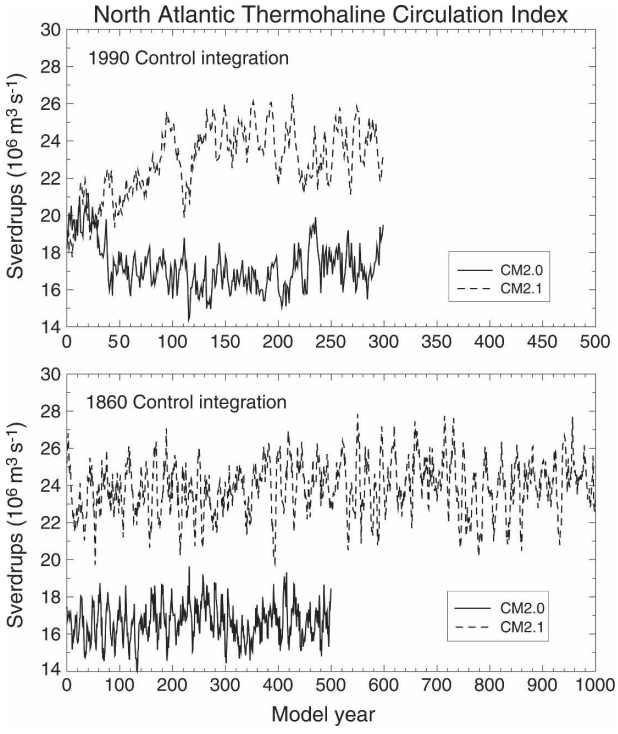

FIG. 8. Time series of the simulated North Atlantic THC (Sv). Index is defined for each year as the maximum value of the meridional overturning streamfunction in the Atlantic Basin between 20° and 80°N, and the surface to 5500-m depth. A recent observational estimate is 18 Sv (Talley et al. 2003). (top) 1990 and (bottom) 1860 control integrations. The values of the THC index plotted here depend on the precise definition of the THC index used. If the index were defined as the maximum value at 20°N from the surface to 5500-m depth, the mean THC values over years 101–200 would be 15.2 for the CM2.0 1990 control, 15.1 for the CM2.0 1860 control, 18.2 for the CM2.1 1990 control, and 18.4 for the CM2.1 1860 control. The differences between the values plotted in Fig. 8 and the values for 20°N indicate some recirculation within the North Atlantic.

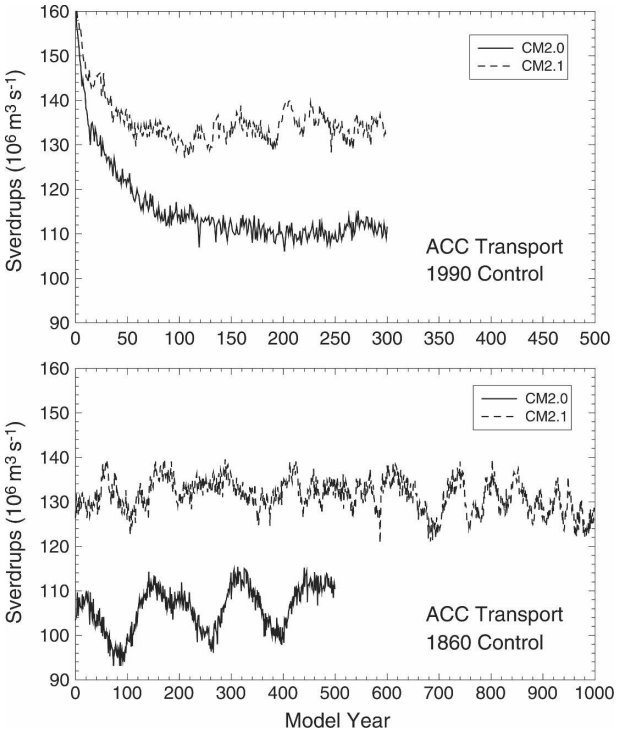

FIG. 9. Time series of ACC, defined as vertically integrated mass transport (Sv) across the Drake Passage (68.5°W). (top) 1990 and (bottom) 1860 control integrations of CM2.0 and CM2.1. Cunningham et al. (2003) provide an observational estimate of 134 Sv, but there is considerable uncertainty in this value.

sphere, with larger errors in CM2.0. The midlatitude cold biases in CM2.0 are related to both an equatorward shift of the westerlies and extensive low cloudiness, and low values of shortwave radiation incident upon the surface. These issues will be explored further in the next section. Both coupled models have relatively small errors in the Tropics, with a tendency for negative SST biases along the cold tongue in the tropical Pacific, and positive biases off the west coasts of the Americas and Africa. The region with the largest cold anomaly in the North Atlantic is related to errors in the location of the Gulf Stream and North Atlantic current. In these regions of extreme surface temperature gradients, even modest errors of a few degrees of latitude or longitude in the position of these currents can generate very large errors in the SST distribution. The bias patterns for the 1860 control integration (not shown) are generally similar, with a cooling of 0.5–1 K relative to the 1990 control integrations.

The overall error pattern does not vary much throughout the course of the integrations, as demonstrated in Fig. 12 by the time series of rmse of 20-yr low-pass-filtered SST. For both 1990 control integrations, there is an initial increase over the first several decades in the global rmse associated with an initial cooling trend (see Fig. 3a). Thereafter, the rmse values are steady or decline slowly, reflective of the gradual warming of the models associated with a positive radiative imbalance. The relative stability in time of the errors is encouraging and demonstrates a very stable simulation of the climate system.

Maps of the errors in the simulation of annual-mean SSS are shown in Fig. 13 for both CM2.0 and CM2.1. With the exception of the Arctic, there is a tendency for a fresh surface bias in CM2.0, with a notable fresh bias in the northwest part of the North Atlantic. The overall tendency is considerably reduced in CM2.1, and the reasons for the improvement were discussed in section 3.

Sea ice extent is shown in Fig. 14. In March, there is

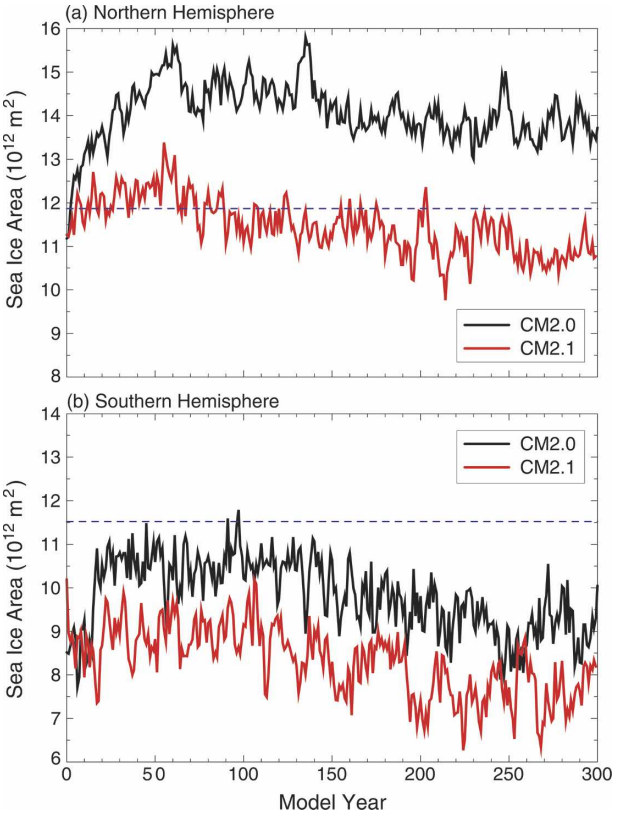

FIG. 10. Time series of annual-mean sea ice area (10^{12} m^2) for the 1990 control runs. Observational estimates for the climatological annual-mean values are shown by the dashed blue lines (from Cavalieri et al. 2003): (a) NH and (b) SH. Black represents CM2.0, and red represents CM2.1.

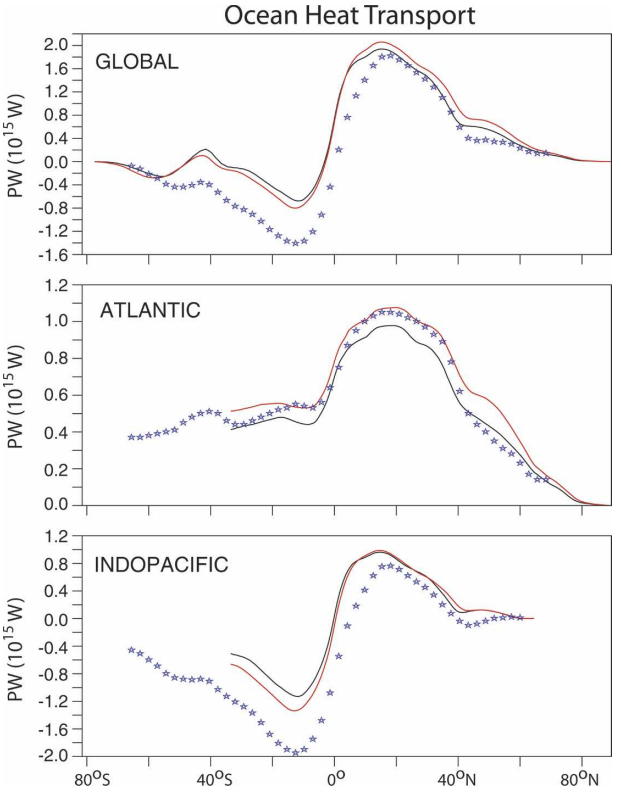

FIG. 11. Simulated northward oceanic heat transport (PW). Black line is for CM2.0 1990 control integration, and red line is for CM2.1 1990 control integration. Asterisk symbols denote observational estimates based on Trenberth and Caron (2001).

a tendency for both models to have excessive extent in the NH, particularly in the North Pacific. One factor related to this bias is insufficient solar radiation incident at the surface, particularly during the summer months. This distorts the seasonal cycle, leading to an earlier and more prolonged cooling season and allowing excessive sea ice growth. Although both models have excessive sea ice extent in the North Atlantic, there is a notable improvement in CM2.1. This improvement is related to the use of a lower horizontal viscosity in OM3.1, thereby enhancing the subpolar gyre in the North Atlantic and associated heat transports. In September, there is too little sea ice in the NH, particularly in CM2.1. Analyses have shown that the melt season starts too early, with the result that albedos decrease too early in the melt season, resulting in relatively low albedos during the peak of insolation. In spite of the extensive sea ice extent in winter, the Arctic sea ice is quite thin in all seasons, which may adversely affect projections of Arctic sea ice change under increasing greenhouse gas concentrations. In the SH, sea ice extent is too small in the SH summer, related to excessive shortwave radiation (shown below). The sea ice biases described above are a serious problem in the model, and are an important area for further model development.

c. *Atmospheric radiation and precipitation*

The greatest SST errors in the coupled models occur at midlatitudes. We believe that these errors result from biases in the absorbed shortwave field that are present in atmosphere-only integrations with observed SSTs, and in this section we perform more analysis of these errors. We do not discuss errors in outgoing longwave radiation, which primarily reflect the precipitation biases discussed below.

The biases in the absorption of shortwave radiation (ASW) in the climate system are shown in Fig. 15. (Absorbed shortwave is defined as downward minus upward shortwave radiation and is shown here for the top of the atmosphere.) The middle two panels show results from CM2.0 and CM2.1, respectively. The bottom two panels show results from AM2.0/LM2.0 and AM2.1/

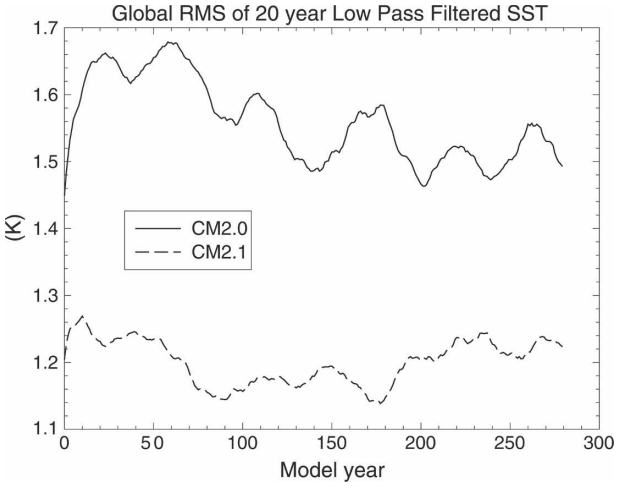

FIG. 12. Time series of global rmse for 20-yr low-pass-filtered SST. This is calculated by first performing a 20-yr low-pass filter on the SST (K) time series, and then computing the rmse each year between the simulated SST and the time mean of the Reynolds observed SST dataset.

LM2.1, respectively, when run in Atmospheric Model Intercomparison Project (AMIP) mode (an integration in which SSTs are prescribed based on the observed time series of SSTs over the period 1982–98). The positive ASW errors in the higher latitudes of the Southern Hemisphere are clearly present in AM2.0/LM2.0 and AM2.1/LM2.1 and are amplified in CM2.0 and CM2.1. These positive ASW errors are a strong contributing factor to the positive SST biases seen in CM2.0 and CM2.1 in the high latitudes of the SH (Fig. 2).

Negative biases in ASW are common over the Northern Hemisphere midlatitudes, and parts of the subtropical Southern Hemisphere oceans. The midlatitude biases in absorbed shortwave induce initial SST biases which are subsequently amplified by positive feedbacks from low clouds (Norris and Leovy 1994) and sea ice albedo feedbacks. This illustrates a common tendency for radiative errors in the AMIP integrations to amplify in the CM2.0 and CM2.1 integrations.

Differences in ASW between the coupled and AMIP integrations are shown in Fig. 16 and further illustrate the amplification of many of the ASW errors after coupling. For both models, the increase in ASW in the high latitudes of the Southern Hemisphere is pronounced, contributing to the positive SST bias. The warmer water leads to an inhibition of low cloudiness, thereby leading to further warming. In CM2.0 (Fig. 16, top) there is an amplification of the negative ASW bias over the middle latitudes of the Northern Hemisphere oceans, contributing to the cold bias. The equatorward shift of the atmospheric westerly winds after coupling contributes to an equatorward contraction of the oceanic subtropical gyre circulations, leading to cooling of near-surface waters in the middle latitudes of the Northern Hemisphere. This cooling of surface waters appears to contribute to increased low-level cloudiness, and a further reduction in ASW. This positive feedback likely contributes to the amplitude of the negative SST biases in the NH middle latitudes.

For CM2.1 there is an increase in ASW for the high latitudes of the SH, similar to CM2.0. However, the amplification of the negative ASW errors in the middle latitudes of the NH is much smaller in CM2.1. A contributing factor is the poleward displacement of the atmospheric westerlies in CM2.1 relative to CM2.0, leading to a poleward displacement of the oceanic gyre circulation, and warmer near-surface waters in the middle latitudes of the NH, which leads to reduced low-level cloudiness in CM2.1 relative to CM2.0. In the North Atlantic, an additional contribution may come from the reduction of oceanic viscosity, which leads to a stronger subpolar gyre circulation in the ocean, and warmer near-surface waters in the North Atlantic, again leading to reduced low-level cloudiness in CM2.1 relative to CM2.0.

The simulation of annual-mean precipitation is shown in Fig. 17. The primary patterns and amplitudes of observed precipitation are reproduced well in both CM2.0 and CM2.1. As was the case with ASW, the patterns of biases in the simulation of precipitation in the atmosphere models (AM2.0/LM2.0 and AM2.1/LM2.1) are present in the coupled models (CM2.0 and CM2.1), but with typically larger amplitudes. A primary deficiency of both models is the tendency to form a double intertropical convergence zone (ITCZ) in the eastern tropical Pacific, as well as in the tropical Atlantic. This bias is more pronounced in CM2.1 than CM2.0. A serious deficiency is the lack of precipitation over the Amazon Basin, which is somewhat worse in AM2.1/LM2.1 and CM2.1 than in AM2.0/L2.0 and CM2.0. This error is generally larger in the coupled models than in the atmosphere-only models. This results in low river outflow from the northern part of South America and contributes to the positive sea surface salinity biases in adjacent regions of the eastern Pacific and tropical Atlantic. Both coupled models tend to have excessive precipitation over the Indonesian Maritime Continent region.

d. Atmospheric circulation and temperature

The errors in simulation of annual-mean surface air temperature (SAT) are shown in Fig. 18 (observational data from Jones et al. 1999). The NH cold bias in CM2.0 is considerably moderated in CM2.1, for reasons previously discussed. A particularly important mechanism

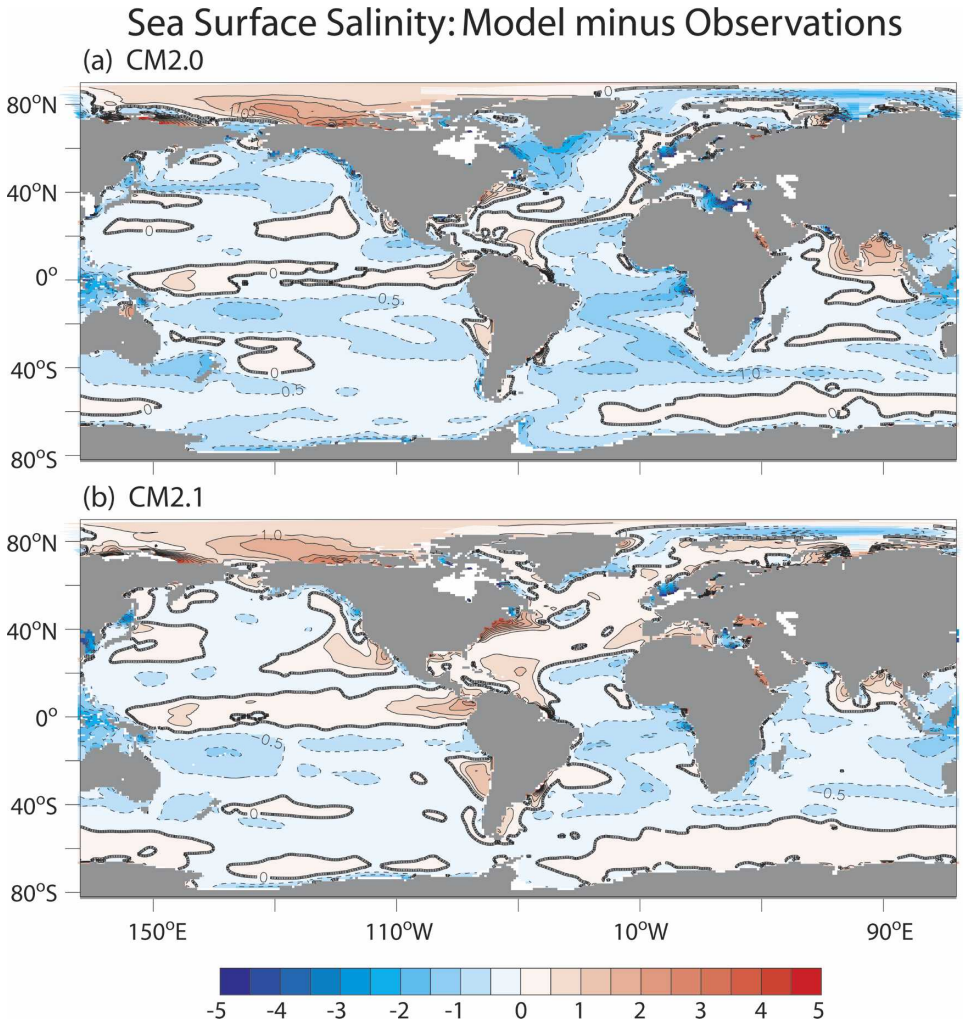

FIG. 13. Errors in simulation of SSS (psu) for the 1990 control integrations. These are constructed as the simulated SSS field minus an observational estimate (Steele et al. 2001). (a) CM2.0 and (b) CM2.1.

for the warming over NH continents is the change in the land model described in section 2.

The distribution of sea level pressure is shown in Figs. 19 and 20. There is a persistent bias with sea level pressure (SLP) values that are too large over the Arctic. This tendency is reduced in CM2.1, particularly in June–August (JJA). This improvement contributes to an improved spatial distribution of sea ice thickness in CM2.1 relative to CM2.0 (not shown). During December–February (DJF) the equatorward displacement of the westerly winds in the SH is quite evident from the dipole structure of SLP errors in CM2.0. This is reduced in CM2.1, consistent with the improved wind pattern.

The vertical distribution of zonal-mean temperature is shown in Fig. 21. Differences between CM2.0 and CM2.1 are small, with both having a tropospheric cold bias. These biases are similar to those appearing in the AMIP integrations, indicating that atmospheric processes are primarily responsible for these biases. The cold bias in CM2.1 is slightly smaller than in CM2.0, with the exception of the Antarctic upper troposphere.

The vertical distribution of observed annual-mean, zonal-mean zonal winds (top panel) and simulation errors relative to the NCEP–NCAR reanalysis (bottom four panels) are shown in Fig. 22. For CM2.0 (middle left panel), the equatorward shift of the westerlies relative to the AM2.0/LM2.0 model (bottom left panel) is clear from the dipole pattern of the errors, with westerly errors on the equatorward side of the dipole. This is present in both hemispheres but is particularly pronounced in the Southern Hemisphere, with errors exceeding 4 m s^{-1} in the upper troposphere, and exceeding 2 m s^{-1} near the surface. The same general structure of bias exists in AM2.1/LM2.1, but it is considerably

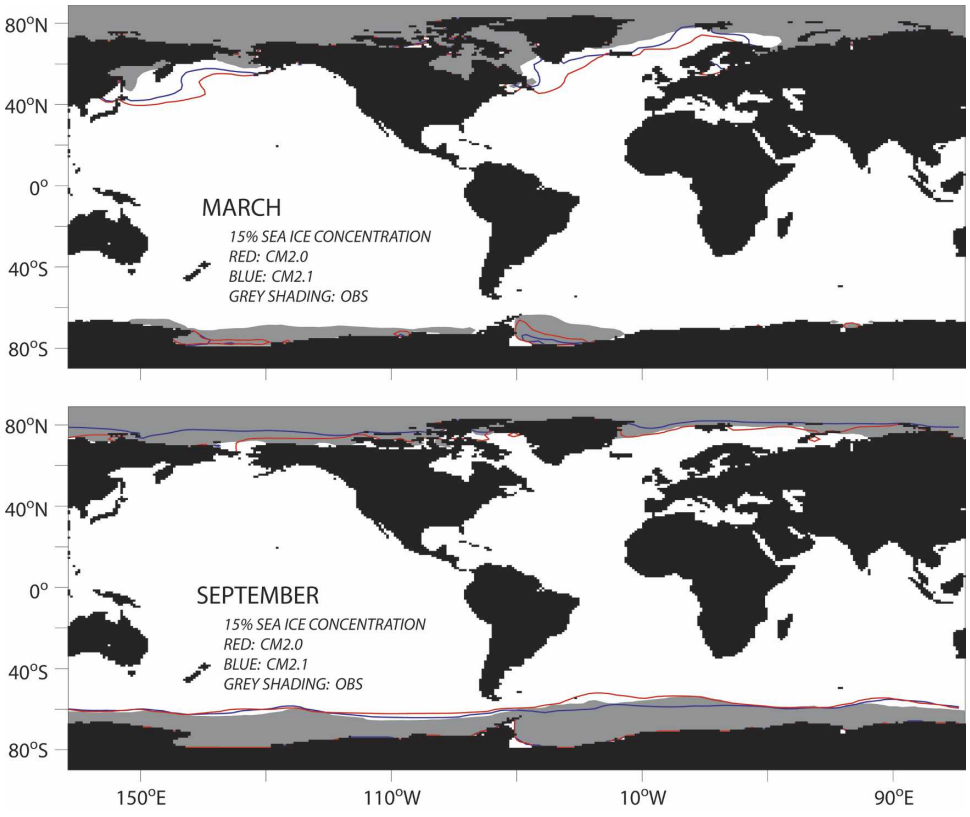

FIG. 14. Simulated and observed sea ice extent for (top) March and (bottom) September. The red (blue) lines indicate extent for CM2.0 (CM2.1), where extent is defined as ice concentrations greater than 15%. Observational values are indicated by the gray shaded areas.

smaller in amplitude. This equatorward drift of the jets is greatly diminished in CM2.1, with profound consequences for water mass properties of the Southern Ocean (Part II). In the Northern Hemisphere, this change accounts for a more poleward subtropical gyre circulation in the North Pacific, substantially reducing some of the negative SST biases. This is clearly inferred from the more poleward location of the zero wind stress curl line in the North Pacific for CM2.1, shown in Fig. 1

To examine the simulated stationary wave pattern, maps of the departures from the zonal mean of the 500-mb geopotential height field for NH winter (DJF) were constructed and are shown in Fig. 23. One of the largest circulation deficiencies in these models is in regard to the stationary wave pattern over North America during this season. Specifically, the trough over northeastern North America is much weaker than observed, leading to a zonal bias in the time-mean flow in that region. This problem is apparent in the AMIP integrations but is amplified in the coupled integrations and is somewhat worse in CM2.1 than in CM2.0. Over the Eurasian and Pacific sectors, the stationary wave pattern for both models is in relatively good agreement with observations. Notable biases are a southward displacement of the ridge over western Europe, and an enhanced amplitude of the trough along the east coast of Asia. Although the stationary wave pattern in CM2.1 during this season is somewhat worse than in CM2.0, it is worth noting that the NH stationary wave pattern for all other seasons is improved on average in CM2.1 relative to CM2.0.

5. Variability characteristics

A few of the characteristics of model-simulated interannual variability are presented in this section (decadal and longer-scale variability will be investigated in future papers). The characteristics of the El Niño–Southern Oscillation phenomenon simulated in these models are presented in Part III. More detailed analyses of other phenomena will be the subject of future papers.

A gross measure of the overall variability characteristics is provided by computing the standard deviation of annual-mean surface temperature at each grid point. For this, we use SST over ocean points and surface air temperature over continental regions. Maps of these

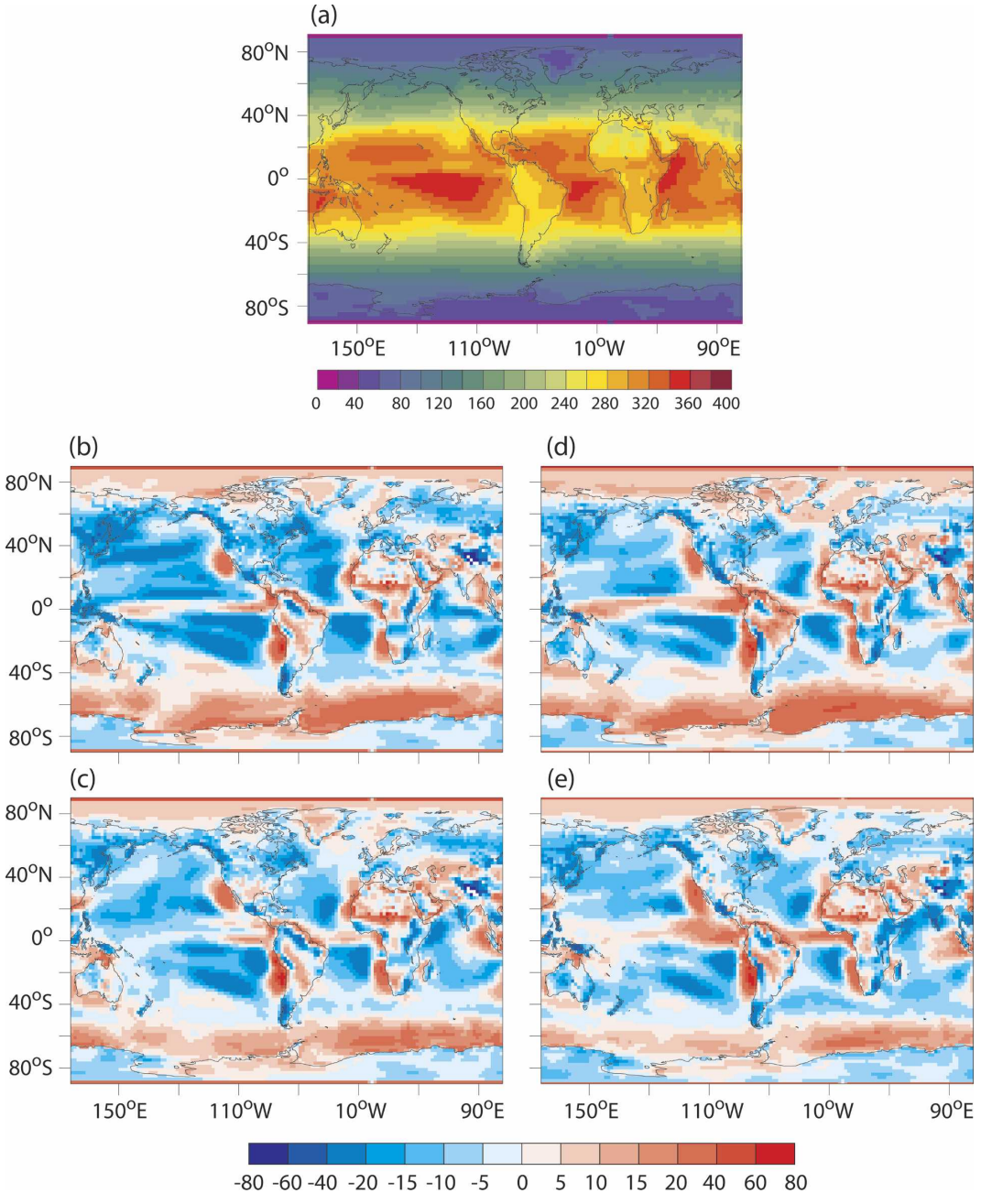

FIG. 15. Observed and simulated annual-mean ASW at the TOA (W m^{-2}). (a) Observational estimate from the Earth Radiation Budget Experiment (ERBE; Harrison et al. 1990). (b) 1990 control integration of CM2.0 (years 101–200) − observations. (c) AM2.0/LM2.0 − observations, where the AM2.0/LM2.0 output is from a 17-yr AMIP integration. (d) Same as in (b), but for CM2.1. (e) Same as in (c), but for AM2.1/LM2.1.

quantities are shown in Fig. 24 for CM2.0 and CM2.1, as well as for the observations. The model fields are based on years 101–200 from CM2.0 or CM2.1. The observed field is based on years 1949–2003 from the HadCRUT2v dataset (the acronym combines "Hadley Centre" with "Climatic Research Unit," and the "v" denotes variance adjustment; for further information see http://www.cru.uea.ac.uk/cru/data/temperature/), which combines the land surface air temperature dataset of Jones and Moberg (2003) with the Hadley Centre sea surface temperature dataset (HadSST1; Parker et al. 1995; Rayner et al. 2003) where variance adjustments have been applied to both land and ocean data (see Jones et al. 2001). A linear trend was removed

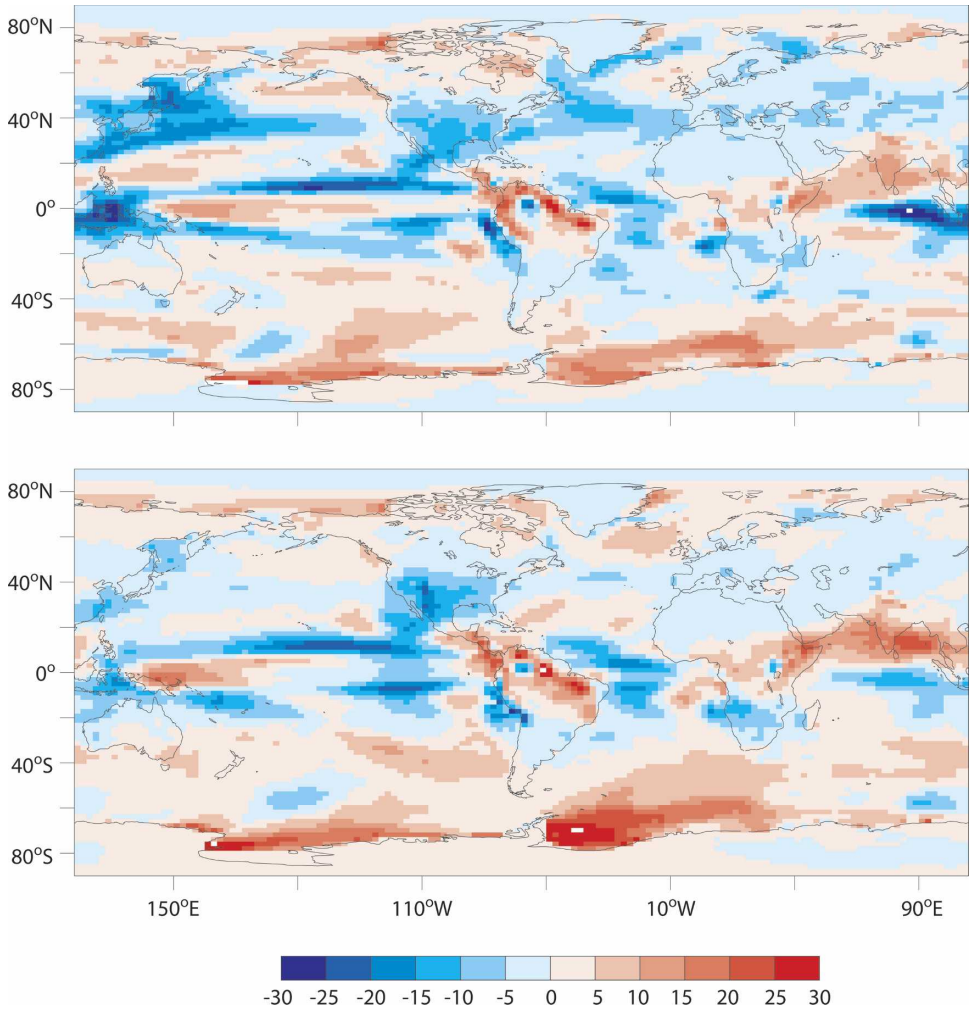

FIG. 16. Differences in annual-mean ASW at the TOA (W m^{-2}) between the coupled models and the atmosphere-only models, computed as ASW in the coupled model minus ASW in the atmosphere-only model. Positive values indicate an increase in ASW in the coupled model relative to the atmosphere-only model. (top) CM2.0 − AM2.0 and (bottom) CM2.1−AM2.1.

from all time series before computing the standard deviations. Similar comparisons for earlier GFDL coupled climate models are shown in Manabe and Stouffer (1996) and Delworth et al. (2002).

The model fields have some broad pattern resemblance with the observations, including enhanced variability over land regions compared to most oceanic regions, and over the El Niño region of the tropical Pacific (although the maximum in the observations is located near the coast, in contrast to the model results). The enhanced variability over land is consistent with the reduced effective thermal inertia of the land surface compared with the ocean. A notable shortcoming of the simulations is the tendency for excessive variability over many land and ocean regions. CM2.1 shows some areas of improved variability simulation compared with CM2.0. For example, the regions of unrealistically large SST variability just east of Japan and south of Greenland in CM2.0 appear less pronounced in CM2.1. On the other hand, in the equatorial Pacific, CM2.1 has larger (less realistic) interannual SST variability than either CM2.0 or the observations (except near the coast of South America); both models displace the region of El Niño–related variability to the west, farther from the South American coast than in the observations. Various aspects of the models' El Niño simulations are discussed in more detail in Part III. The mechanism responsible for the excessive local surface temperature variability in the model simulations shown in Fig. 24 is a topic of further investigation.

Apart from ENSO, the dominant patterns of global-scale climate variability are the annular modes in both hemispheres. The Northern Annular Mode [NAM, or Arctic Oscillation (AO)] is the leading climate variabil-

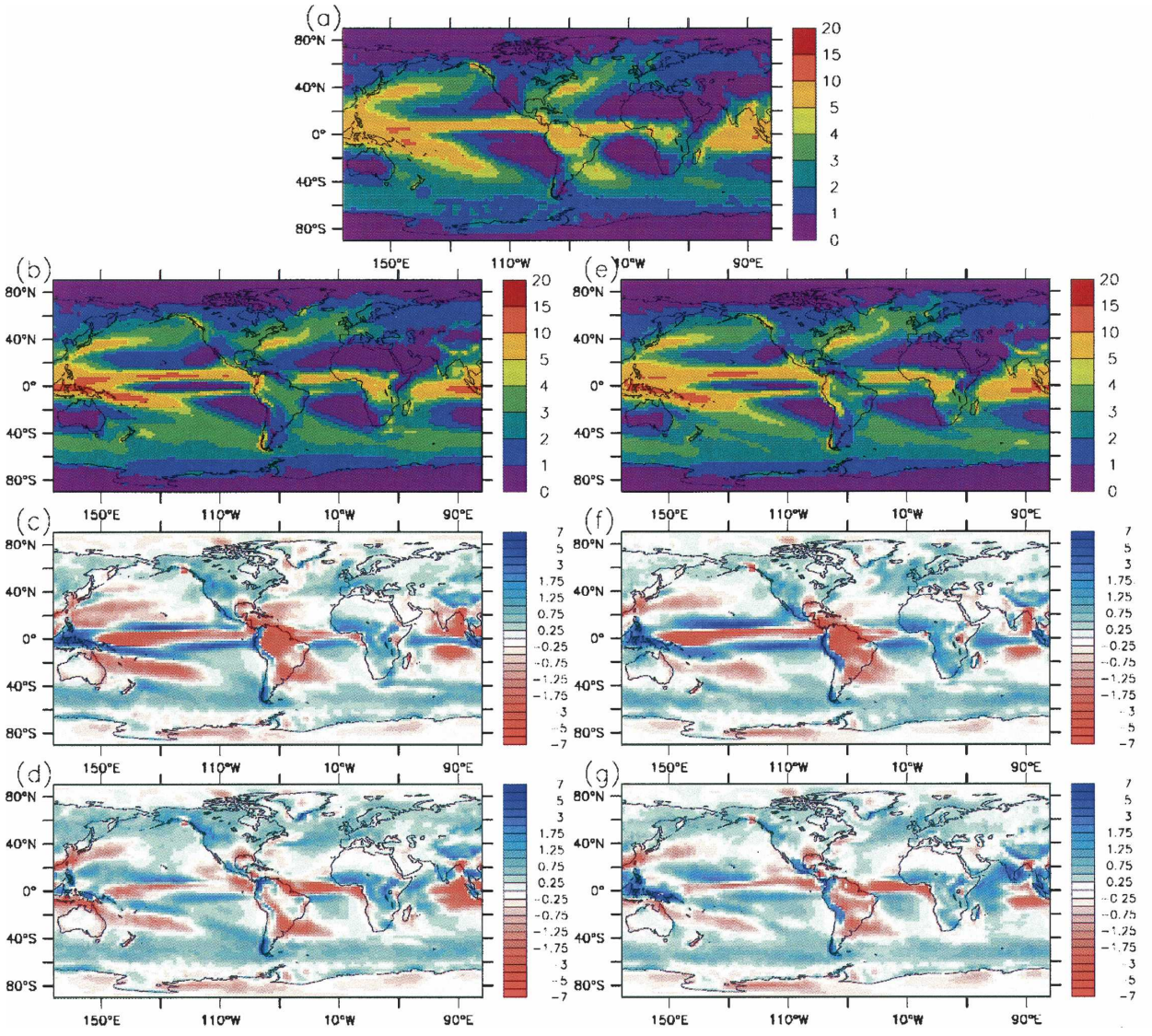

FIG. 17. Annual-mean precipitation (mm day^{-1}). (a) Observational estimate (Xie and Arkin 1997), (b) 1990 control integration of CM2.0 (years 101–200), (c) CM2.0 (years 101–200) − observations, (d) AM2.0/LM2.0 (mean of 17-yr AMIP integration) − observations, (e) 1990 control integration of CM2.1 (years 101–200), (f) CM2.1 (years 101–200) − observations, and (g) AM2.1/LM2.1 (mean of 17-yr AMIP integration) − observations.

ity mode on time scales from days to decades over the Northern Hemisphere (Thompson and Wallace 2000; Thompson et al. 2000). The Northern Hemisphere climate change patterns project positively onto the NAM. The distributions of SLP and surface temperature anomalies associated with the NAM are shown in Fig. 25. The amplitudes in SLP and temperature, in units of hectopascals and kelvins, respectively, correspond to one standard deviation of the NAM index. The NAM index, or AO index, is defined as the leading principal component of monthly SLP over the domain from 20° to 90°N. Only the months of November through April are used to calculate the NAM in Fig. 25.

Both CM2.0 and CM2.1 models can realistically capture the NAM SLP dipole anomalies between the Arctic and central North Atlantic, except for an overestimation of the low pressure center near the pole by CM2.1. A pronounced difference is that the simulated high pressure anomaly over the North Pacific is about 2∼3 times as strong as the observations, thus rendering a longitudinally more symmetric NAM SLP distribution in the models. This might also relate to the greater variance of SLP explained by the NAM in the models (31%) than the NCEP–NCAR reanalysis (24%). The NAM pattern for CM2.0 is almost identical to that of AM2 shown in Fig. 17 in GFDL_GAMDT.

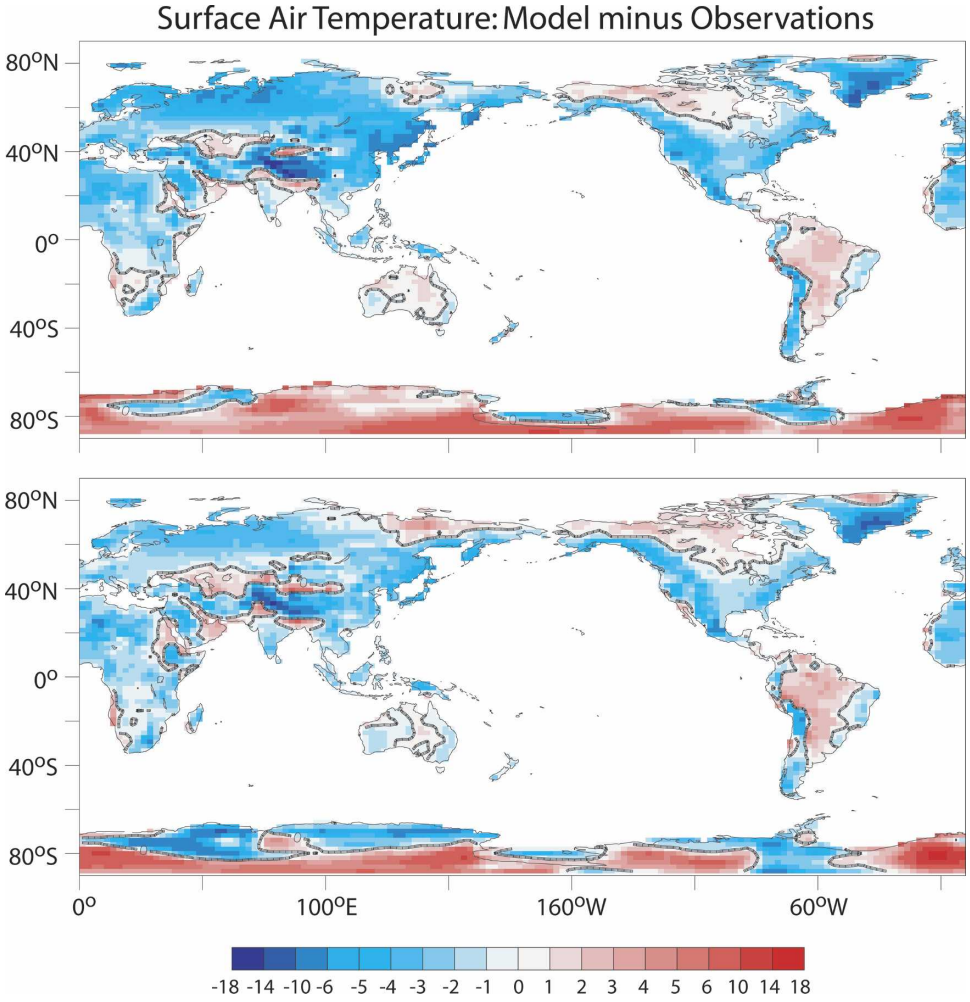

FIG. 18. Errors in simulation of annual-mean SAT (K) over continental regions. The fields plotted are simulated minus observed SATs (from Jones et al. 1999). Blue shading indicates that the simulated temperatures are lower than observed. (top) CM2.0 and (bottom) CM2.1.

The geostrophic winds associated with the SLP dipole anomalies, by advecting the climatological-mean temperature, induce a quadrupole field of temperature anomalies (shown by the shading in Fig. 25) with positive anomalies over southeastern North America and northern Eurasia and negative anomalies over northeastern North America and northern Africa through the Middle East. The primary discrepancy between the simulated and observed temperature anomalies occurs near Alaska, with larger negative temperature anomalies in CM2.0 and CM2.1 than observed. This is consistent with the larger SLP anomalies and the associated SLP gradients over the North Pacific in the simulations.

The Southern Hemisphere counterpart of the Annular Mode is presented in Fig. 26. The calculation of the Southern Annular Mode [SAM, or referred to as Antarctic Oscillation (AAO)] is similar to the NAM except that monthly data for all months are used and that only data later than 1978 are used for the observational analyses. The NCEP–NCAR reanalysis is less reliable in the Southern Hemisphere during the earlier decades. Again, the spatial structure and amplitudes of SLP and surface temperature anomalies associated with the SAM are well simulated by CM2.0 and CM2.1. CM2.1 performs discernibly better than CM2.0 with respect to the strength of low pressure anomalies over Antarctica, and the temperature distribution near the Antarctica Peninsula. A significant difference is that the vertical structure of zonal-mean zonal wind of the SAM for CM2.1 is in much better agreement with observations, with westerly anomalies centered at 60°S and easterly anomalies centered at 40°S (not shown). In CM2.0, the zonal wind structure associated with the SAM is displaced equatorward by 2~3 degrees, which is due to the

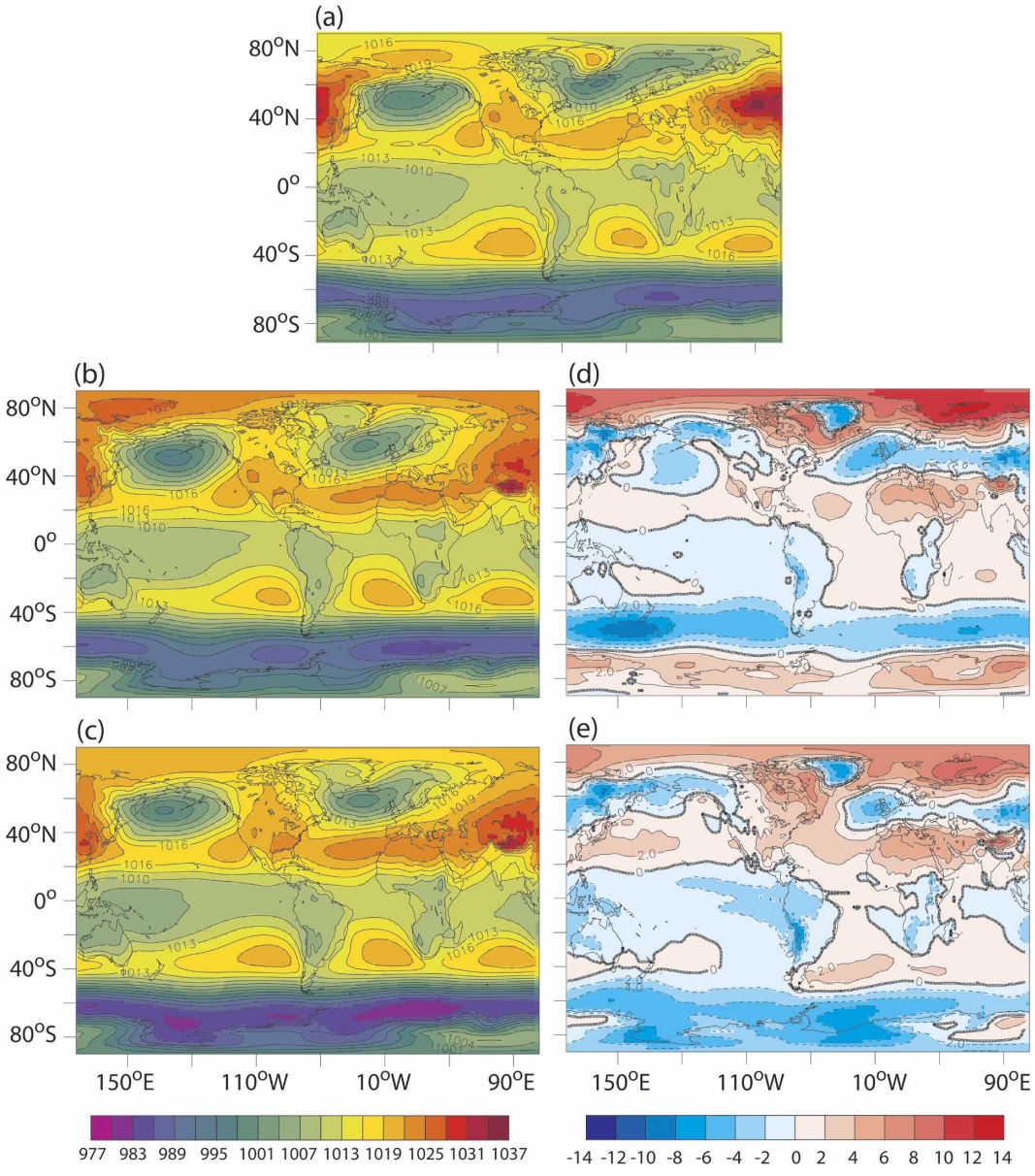

FIG. 19. Observed (NCEP–NCAR reanalysis) and simulated SLP (hPa) for DJF. (a) Observations, (b) SLP in CM2.0, (c) SLP in CM2.1, (d) SLP in CM2.0 − observations, and (e) SLP in CM2.1 − observations.

fact that the climatological-mean midlatitude westerly winds in the model are located equatorward of their observed position (see Fig. 22), and that the Annular Mode and the midlatitude storm track tend to follow the climatological-mean westerly winds. The improved simulation of the SH midlatitude westerlies in CM2.1 results in an improvement in the SAM simulation.

6. Discussion and plans

In this paper, the formulation and simulation characteristics of two versions of a global coupled climate model developed at GFDL have been presented. The models, called CM2.0 and CM2.1, do not employ flux adjustments. Multiple-century simulations have been completed with both models, and the simulated climates are stable and highly credible when compared to observations. CM2.0 is being used in experimental seasonal to interannual forecasting and shows good skill in predicting ENSO events (hindcast evaluation metrics and real-time forecasts are available online at http://www.gfdl.noaa.gov/~rgg/si_workdir/Forecasts.html). This same model is used for multicentury climate change projections.

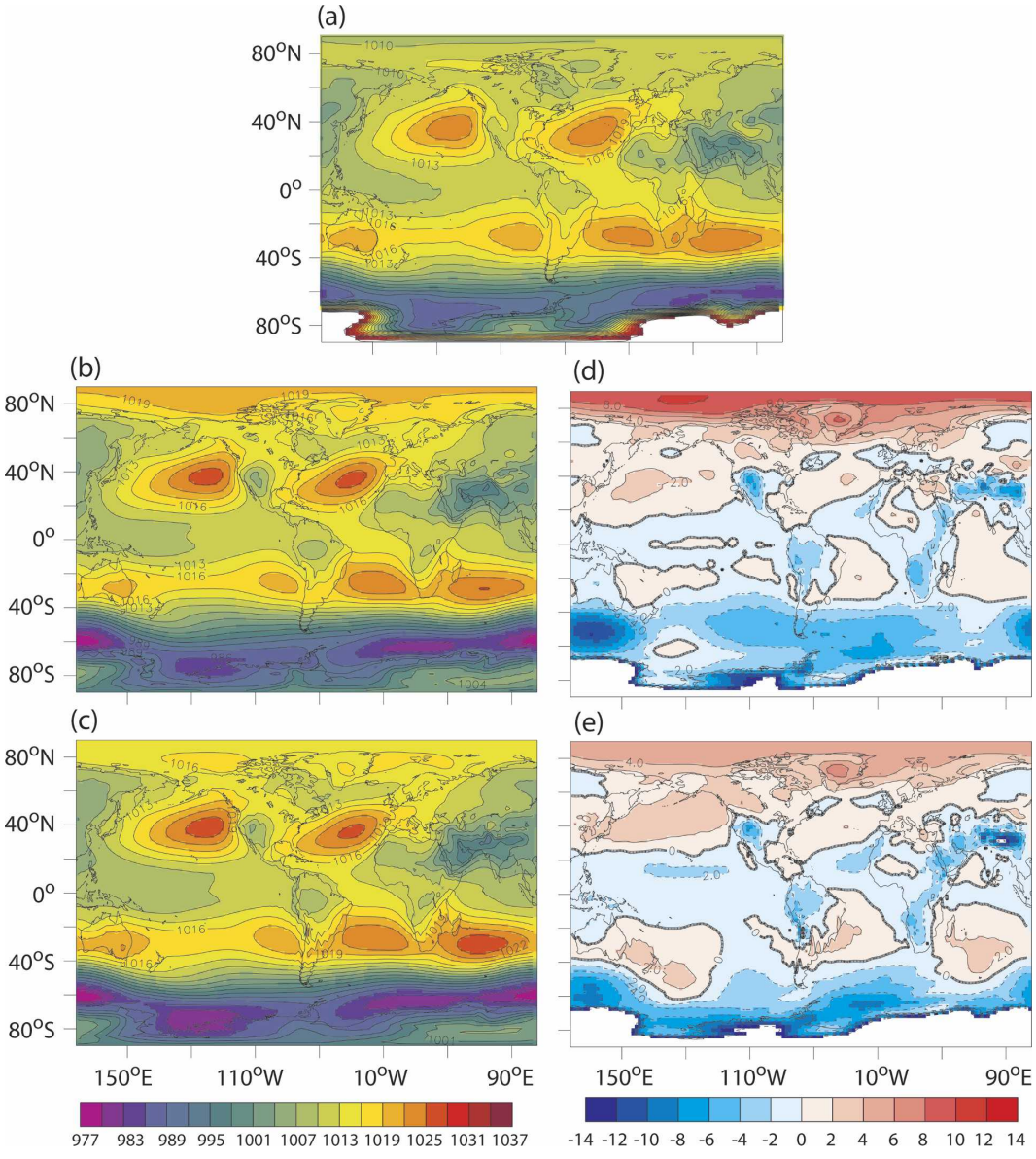

FIG. 20. Same as in Fig. 19, but for JJA. The color shading is allowed to go off scale around Antarctica where observational values of SLP are less reliable.

As described in section 2, the CM2.0 atmospheric component uses a B grid dynamical core, and the CM2.1 atmospheric component uses a finite volume (FV) dynamical core. The FV core leads to an improved simulation of the midlatitude westerly winds after coupling, and overall lower SST biases. *This difference in the midlatitude westerly winds, and associated reduction in overall biases, is the primary reason why two coupled models have been developed and used.* Additional differences between CM2.0 and CM2.1 include (i) a retuning of the clouds to increase the net shortwave radiation at the surface in CM2.1 relative to CM2.0; (ii) a change in the land model to suppress evaporation when soil is frozen at a depth of 30 cm—this reduces late spring evaporation at higher latitudes of the Northern Hemisphere, thereby reducing cloudiness and increasing net surface shortwave radiation in CM2.1 relative to CM2.0; and (iii) the use of a lower extratropical horizontal viscosity in the CM2.1 ocean component—this reduces sea ice in the North Atlantic, thereby substantially reducing the cold bias seen there in CM2.0. *These overall results highlight the crucial importance of the simulation of surface fluxes (heat, water, and momentum) for the drift characteristics of coupled models.*

As described more fully in a companion paper (Part

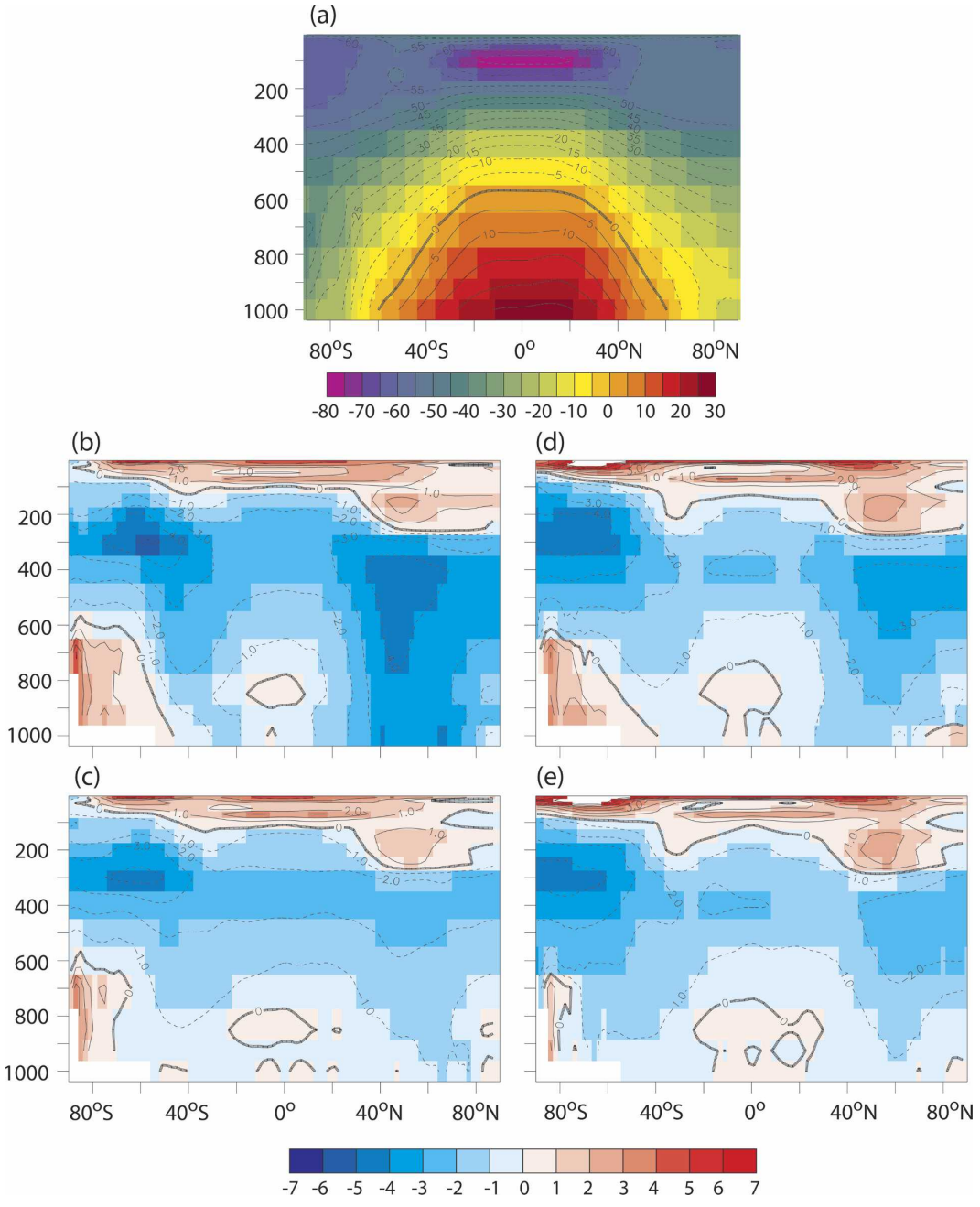

FIG. 21. Annual-mean, zonal-mean air temperature (°C). (a) Observational estimates from the NCEP reanalyses, (b) CM2.0 − NCEP, (c) AM2.0 − NCEP, (d) CM2.1− NCEP, and (e) AM2.1−NCEP.

IV) the climate sensitivities (defined by coupling the atmospheric component of the coupled models to a slab ocean, and calculating the equilibrium response of global-mean surface air temperature to a doubling of atmospheric CO_2) of CM2.0 and CM2.1 are 2.9 and 3.4 K, respectively. Output from a suite of simulations using these models is freely available on the Internet (see http://nomads.gfdl.noaa.gov/).

The models described here are the result of a substantial, multiyear effort at GFDL to develop a new generation of modeling tools. This effort tried to foster a unified approach to model development, in which the development of various component models occurred in close coordination. The strong interactions and feedbacks between model components within the coupled climate system suggest that such a holistic approach to

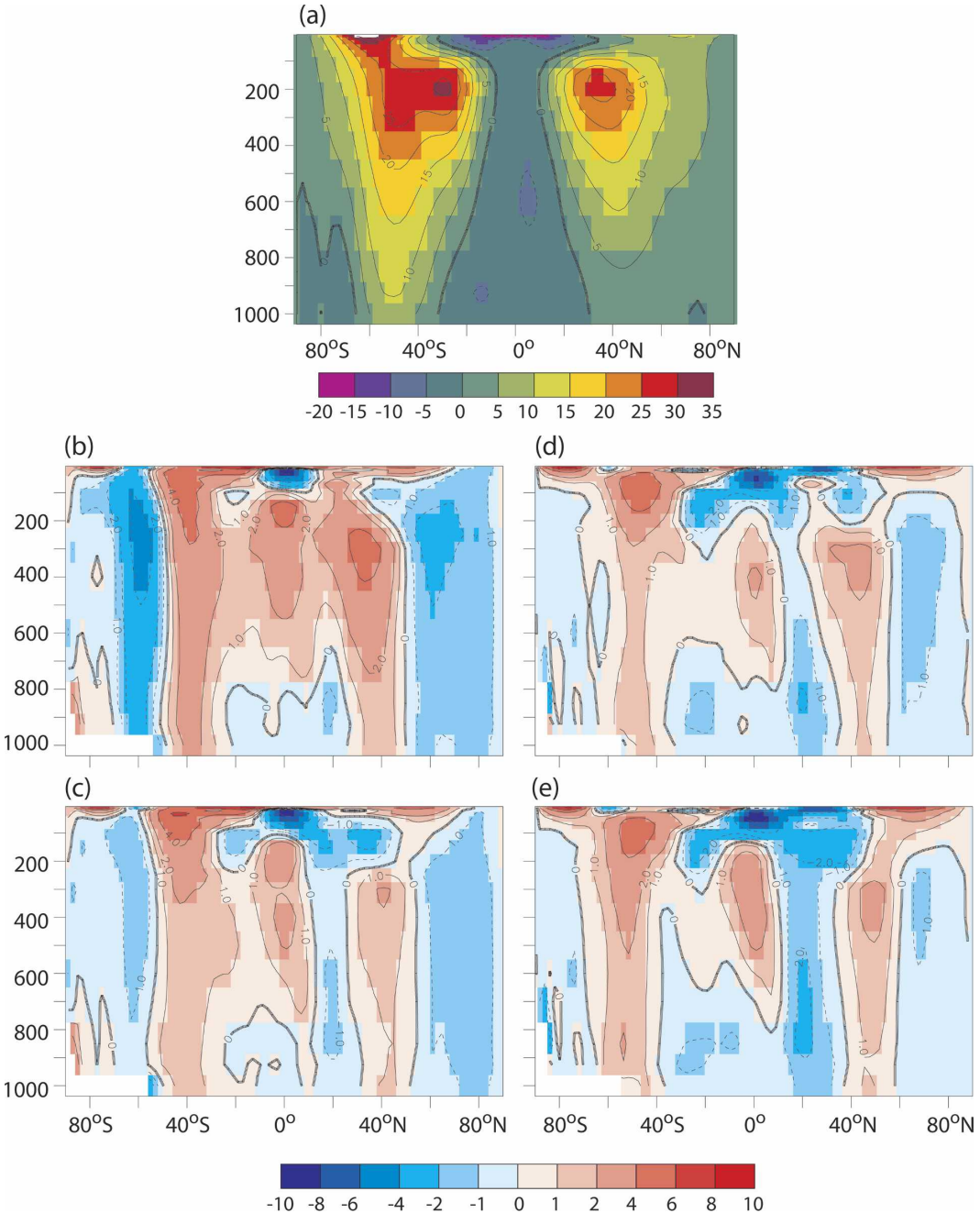

FIG. 22. Annual-mean, zonal-average of zonal wind (m s^{-1}). (a) Observational estimates from the NCEP reanalysis, 1958–97, (b) CM2.0 − NCEP, (c) AM2.0 − NCEP, (d) CM2.1−NCEP, and (e) AM2.1− NCEP.

model development—in which model components are not developed in isolation, but rather in parallel, with strong levels of interaction—can be very valuable. The development process also had a substantial emphasis on various aspects of software engineering, including a paradigm (the Flexible Modeling System; http://www.gfdl.noaa.gov/fms) whereby the details of machine architectures are contained in a layer separate from that used by scientists in developing model physics.

There are several key foci of ongoing model development efforts. One of the key decisions made during the course of this development has been the adoption of the finite volume dynamical core for further atmospheric model development. The use of this core has led to improvements in several aspects of the coupled

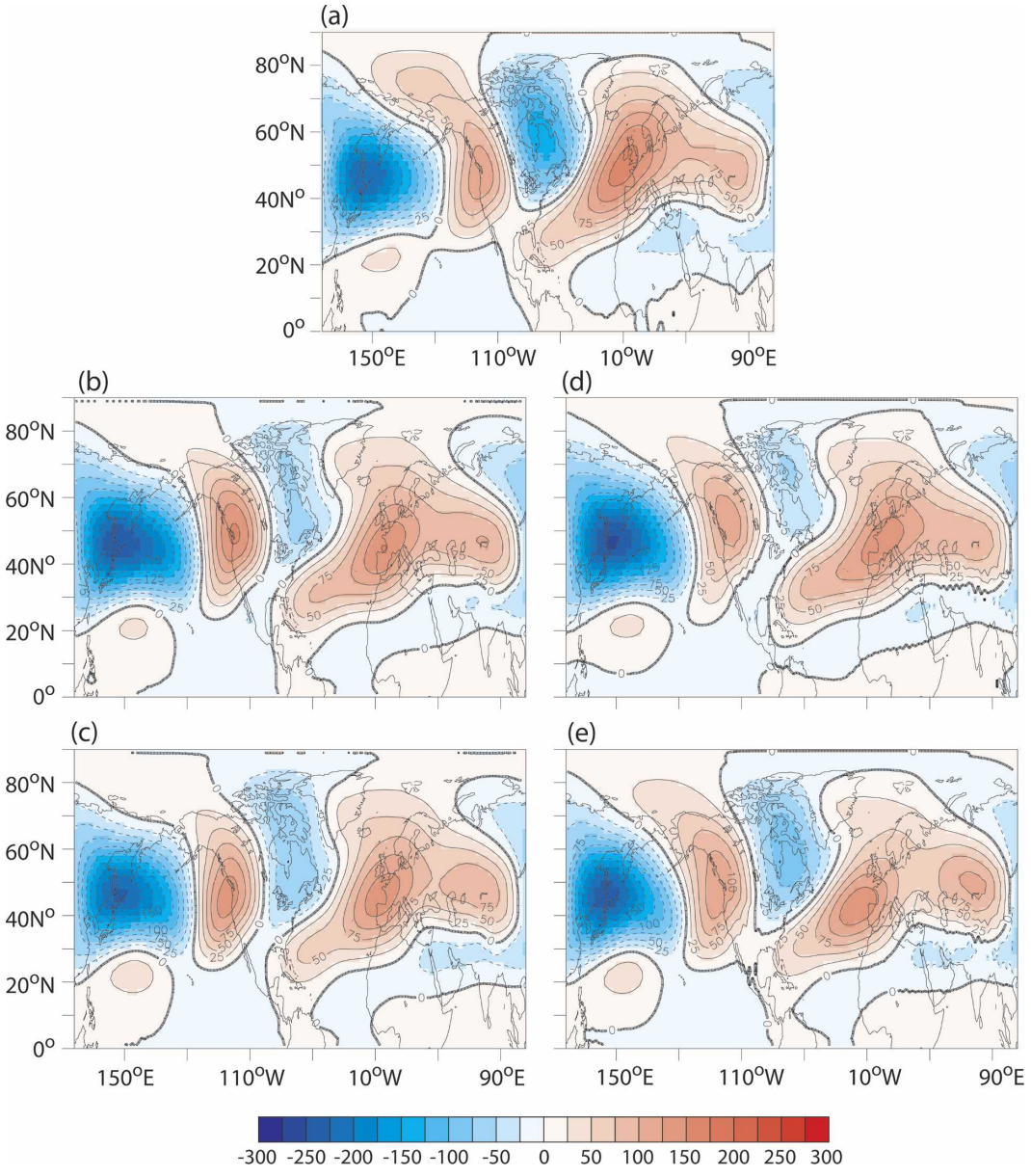

FIG. 23. Stationary eddy fields for geopotential height (m) at 500 mb during NH winter (DJF), defined as the 500-mb geopotential height at each grid point minus the zonal mean. (a) Observational estimates from NCEP–NCAR reanalysis, 1958–97, (b) CM2.0, (c) AM2.0, (d) CM2.1, and (e) AM2.1.

model solution; in addition, for our simulations this core is more computationally efficient. Central to ongoing modeling work will be the development and evaluation of new physical parameterizations that might address some of the known shortcomings of the models. One crucial topic is developing and incorporating a more realistic treatment of the role of aerosols in the climate system. A more comprehensive land model has been developed and will soon be implemented in our coupled models. This has a more detailed representation of land hydrology and physics, as well as its interaction with terrestrial ecosystems. Ongoing work in convection and cloud parameterizations is crucial for the goal of reducing some of the biases described in this paper. The incorporation of a new convection scheme (Donner et al. 2001) is being evaluated, as are a new anisotropic orographic gravity wave drag scheme and a convectively generated gravity wave scheme. There is extensive work to incorporate atmospheric chemical processes within the models. In addition, a completely

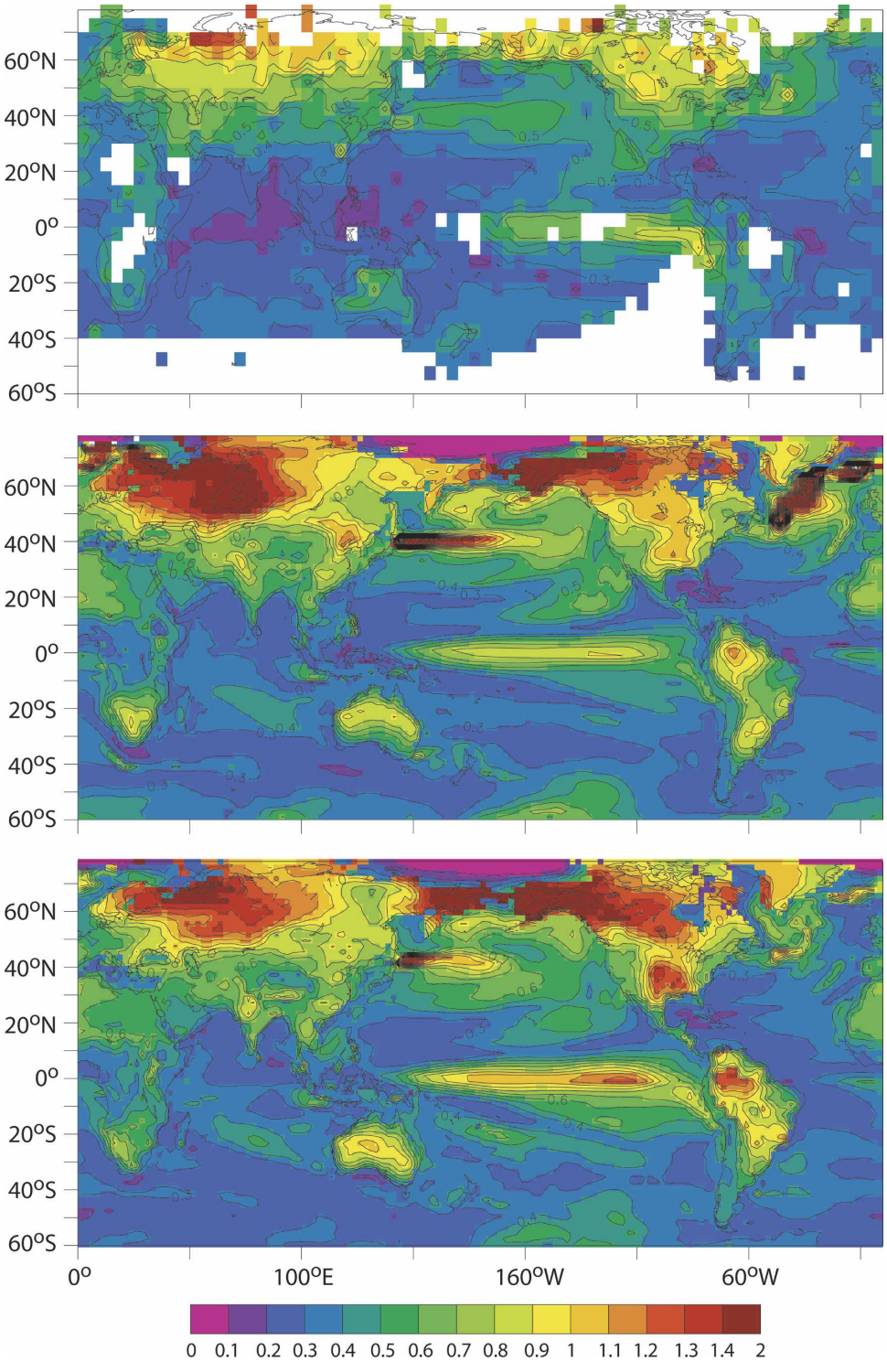

FIG. 24. Maps of standard deviation of annual-mean temperature (K; SST over the ocean and SAT over land). (top) Observational estimates (HadCRUT2v dataset, available online at http://www.cru.uea.ac.uk/cru/data/temperature/), (middle) CM2.0, and (bottom) CM2.1.

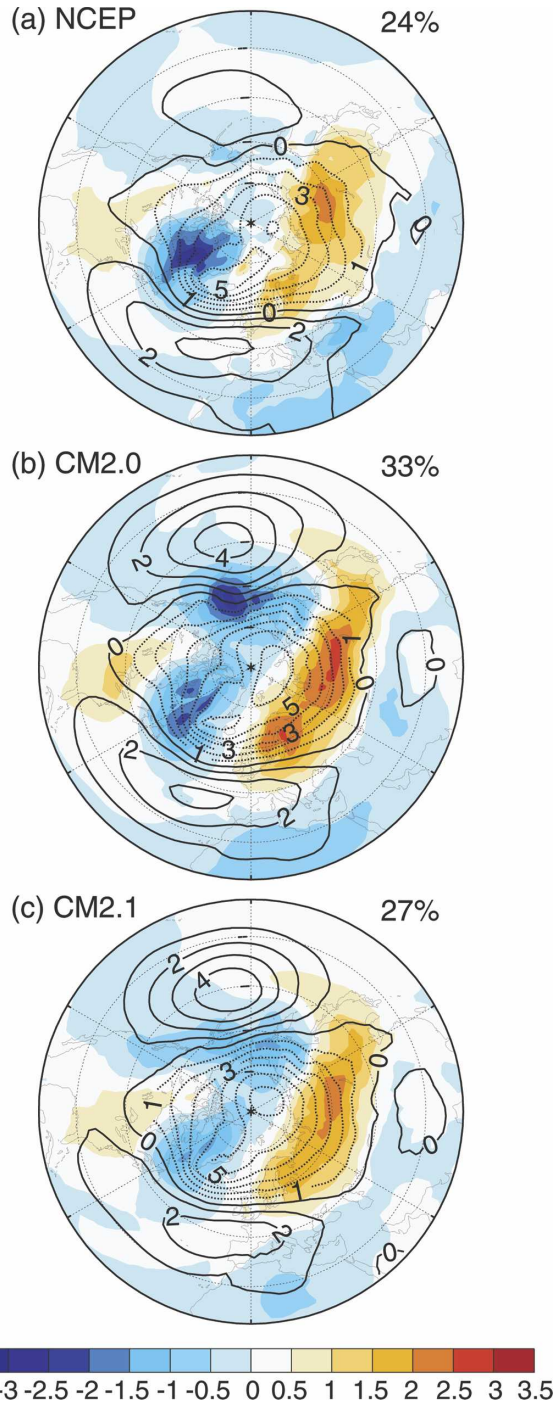

FIG. 25. Spatial pattern of anomalies in SLP (hPa; contours) and 2-m SAT (K; color shading) associated with 1 std dev of the AO index, also referred to as the NAM. The AO index is defined as the first principal component of monthly SLP from November through April for all points north of 20°N. Both SLP and surface temperature patterns are derived from regression against the standardized AO index. (a) Spatial AO patterns for NCEP–NCAR reanalysis using data from 1948 through 2003, (b) similar to (a) but for years 101–200 from CM2.0 control run output, and (c) similar to (a) but for years 51–100 from CM2.1 control run output.

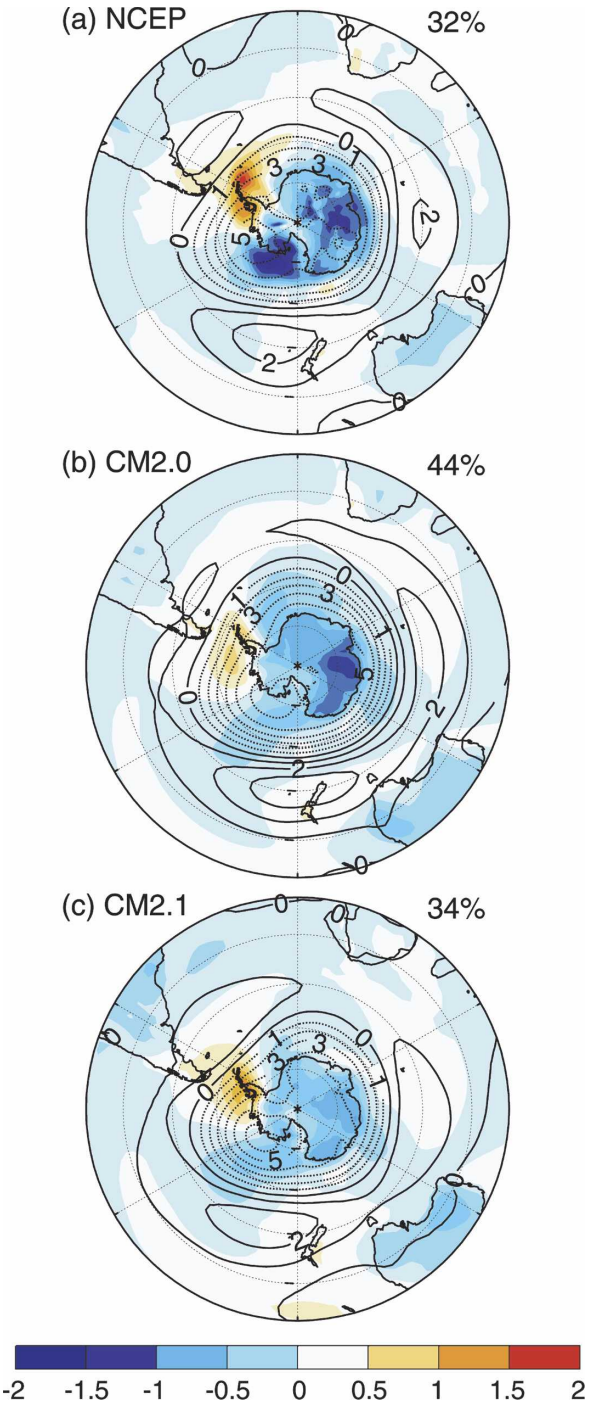

FIG. 26. Same as in Fig. 25, but for the AAO index, also referred to as the SAM. The AAO index is defined as the first principal component of monthly SLP for all points south of 20°S. (a) Same as in Fig. 25a, but for AAO and using data from 1978 to 2003. (b), (c) Same as Figs. 25b,c, but for AAO.

independent ocean model using isopycnal coordinates will soon be available for inclusion as part of the coupled climate model.

New models are currently under development that include higher spatial resolution in both the horizontal and vertical. In particular, the model described in this paper does not have a well-resolved stratosphere; interactions between the stratosphere and troposphere may play a crucial role in climate variability and change, and thus need to be properly resolved.

Extensive efforts are under way to develop a comprehensive Earth System Model that includes interactions between the physical climate system (as represented in CM2.0 and CM2.1), global ecosystems, and global biogeochemical processes.

Acknowledgments. The authors would like to express their appreciation to Dr. Ants Leetmaa, GFDL Director, and Dr. Jerry Mahlman, former GFDL Director, for their enthusiastic support of this project. We also thank Drs. Leo Donner, Steve Garner, Ronald Pacanowski, and two anonymous reviewers for very helpful comments and suggestions. The assistance of the GFDL computational and administrative support services staff is greatly appreciated. The authors wish to acknowledge use of the Ferret program for analysis and graphics in this paper. Ferret is a product of NOAA's Pacific Marine Environmental Laboratory. (Information is available at www.ferret.noaa.gov.)

APPENDIX

The Sea Ice Model: SIS

The CM2 sea ice model prognoses the velocity of the ice pack and the area and thermodynamic properties of ice and snow in five ice thickness categories. The snow layer has no heat capacity. The two ice layers are equally sized. Both have sensible heat capacity, and the upper layer, additionally, has latent heat capacity (brine). The brine content is calculated as a function of ice salinity and temperature as in the Bitz and Lipscomb (1999) model. The salinity of the ice for this purpose is set to mimic the behavior of the Semtner (1976) brine parameterization. A second ice salinity is used for calculating the salt flux between the ice and ocean that accompanies a given water flux. Ice is transferred between the three layers conservatively when there is snowfall, evaporation, melting, freezing, or when the weight of the snow pushes it down below the waterline. For details see Winton (2000). The flux of heat between the ocean and ice bottom is a constant times the ice–ocean temperature difference. The albedo of the ice follows Briegleb et al. (2002) with modifications. Because CM2 does not distinguish between visible and near-infrared surface insolation, the spectral albedos of Briegleb et al. (2002) are combined in a fixed ratio: 53% visible and 47% near infrared. The dry and wet albedos for ice and snow are given in Table A1. Additionally, the Briegleb et al. (2002) scheme has been modified to factor in wet albedos within 10 K of melting temperature rather than 1 K.

TABLE A1. Sea ice model parameters.

Parameter	Value
Ice salinity (for brine content)	0.001
Ice salinity (for salt fluxes)	0.005
Snow albedo (dry/wet)	0.80/0.68
Ice albedo (dry/wet)	0.58/0.51
Ice strength parameters (P^*/c^*)	2.5×10^4 Pa/20
Ice/ocean drag coefficient (c_w)	3.24×10^{-3}
Ice surface roughness length	10^{-4} m
Ocean–ice thermal coupling	240 W m^{-2} K
Ice thickness category boundaries limits	0.1, 0.3, 0.7, 1.1 m

The ice pack motion is calculated from the equation

$$m\left(\frac{\partial \mathbf{v}}{\partial t} + f\mathbf{k} \times \mathbf{v} + g\nabla\eta\right) = \nabla \cdot \boldsymbol{\sigma} + \sum_k c_k[\tau_a + c_w\rho_w|\mathbf{v}_w - \mathbf{v}|(\mathbf{v}_w - \mathbf{v})],$$

where m is the mass of ice and snow, $\mathbf{v}$ is the ice velocity, $\mathbf{v}_w$ is the ocean velocity, g is gravity, η is the modified free surface, $\boldsymbol{\sigma}$ is the ice internal force, c_k is the concentration of ice in the kth category, $\boldsymbol{\tau}_a$ is the wind stress, c_w is the ice ocean coupling coefficient, and ρ_w is the density of seawater. Because the ice and snow weight depress the ocean free surface, η, appearing on the left side of the equation is the ocean free surface plus the water equivalent depth of the ice and snow. The calculation of the ice internal force follows Hunke and Dukowicz (1997) except that 1) standard B grid differencing is used, 2) metric terms are retained in the stress divergence and strain rate tensors, and 3) viscosities are calculated every elastic subcycling time step. The ice internal forces scale with the ice strength

$$P = P^* \sum_k (c_k h_k) \exp\left[-c^*\left(1 - \sum_k c_k\right)\right],$$

following Hibler (1979). An upstream technique is used for advection of the five conservative quantities: ice concentration, snow mass, ice mass, ice upper layer enthalpy, and ice lower layer enthalpy.

The thickness categories are intended to resolve the thin end of the spectrum where ice grows rapidly and melts to form leads (Table A1). The thickest category has no upper limit. Frazil ice from the ocean is added to the thinnest category. After thermodynamics and transport, the categories are adjusted to maintain the ice

within the thickness boundary limits. If the total concentration of ice within a grid cell exceeds one, a pass is made through the ice categories from thin to thick, removing concentration from the individual categories. If the concentration of a category becomes negative, it is combined with the next thicker category. Following this, a pass is made from the thinnest to the thickest category, moving ice that has exceeded its upper-category thickness boundary to the next thicker category. Finally, another pass is made from thick to thin moving ice below its lower category thickness limit to the next thinner category. The movement of ice between categories occurs by converting to conservative quantities, combining, and reconstituting conventional snow and ice properties from the conservative quantities.

REFERENCES

Antonov, J. I., S. Levitus, T. P. Boyer, M. E. Conkright, T. D. O'Brien, and C. Stephens, 1998: *Temperature of the Atlantic Ocean.* Vol. 1, *World Ocean Atlas 1998,* NOAA Atlas NESDIS 27, 166 pp.

Bitz, C. M., and W. H. Lipscomb, 1999: A new energy-conserving sea ice model for climate study. *J. Geophys. Res.,* **104,** 15 669–15 677.

Boyer, T. P., S. Levitus, J. I. Antonov, M. E. Conkright, T. D. O'Brien, and C. Stephens, 1998: *Salinity of the Atlantic Ocean.* Vol. 4, *World Ocean Atlas 1998,* NOAA Atlas NESDIS 30, 166 pp.

Briegleb, B. P., E. C. Hunke, C. M. Bitz, W. H. Lipscomb, and J. L. Schramm, cited 2002: Description of the Community Climate System Model Version 2 Sea Ice Model. 60 pp. [Available online at http://www.ccsm.ucar.edu/models/ccsm2.0/csim/.]

Cavalieri, D. J., C. L. Parkinson, and K. Y. Vinnikov, 2003: 30-year satellite record reveals contrasting Arctic and Antarctic decadal variability. *Geophys. Res. Lett.,* **30,** 1970, doi:10.1029/2003GL018031.

Cooke, W. F., C. Liousse, H. Cashier, and J. Feichter, 1999: Construction of a $1° \times 1°$ fossil fuel emission dataset for carbonaceous aerosol and implementation and radiative impact in the ECHAM-4 model. *J. Geophys. Res.,* **104,** 22 137–22 162.

Cunningham, S. A., S. G. Alderson, B. A. King, and M. A. Brandon, 2003: Transport and variability of the Antarctic Circumpolar Current in Drake Passage. *J. Geophys. Res.,* **108,** 8084, doi:10.1029/2001JC001147.

Delworth, T. L., R. J. Stouffer, K. W. Dixon, M. J. Spelman, T. R. Knutson, A. J. Broccoli, P. J. Kushner, and R. T. Wetherald, 2002: Review of simulations of climate variability and change with the GFDL R30 coupled climate model. *Climate Dyn.,* **19,** 555–574.

Donner, L., C. J. Seman, R. S. Hemler, and S. Fan, 2001: A cumulus parameterization including mass fluxes, convective vertical velocities, and mesoscale effects: Thermodynamic and hydrological aspects in a general circulation model. *J. Climate,* **14,** 3444–3463.

GFDL Global Atmospheric Model Development Team, 2004: The new GFDL global atmosphere and land model AM2/LM2: Evaluation with prescribed SST simulations. *J. Climate,* **17,** 4641–4673.

Ginoux, P., M. Chin, I. Tegen, J. M. Prospero, B. Holben, O. Dubovik, and S. J. Lin, 2001: Sources and distributions of dust aerosols simulated with the GOCART model. *J. Geophys. Res.,* **106,** 20 255–20 273.

Gnanadesikan, A., and Coauthors, 2006: GFDL's CM2 global coupled climate models. Part II: The baseline ocean simulation. *J. Climate,* **19,** 675–697.

Griffies, S. M., M. J. Harrison, R. C. Pacanowski, and A. Rosati, 2003: A technical guide to MOM4. GFDL Ocean Group Tech. Rep. 5, NOAA/Geophysical Fluid Dynamics Laboratory, Princeton, NJ, 295 pp.

——, and Coauthors, 2005: Formulation of an ocean model for global climate simulations. *Ocean Sci.,* **1,** 45–70.

Hamilton, K. P., R. J. Wilson, J. D. Mahlman, and L. Umscheid, 1995: Climatology of the SKYHI troposphere–stratosphere–mesosphere general circulation model. *J. Atmos. Sci.,* **52,** 5–43.

Harrison, E. F., P. Minnis, B. R. Barkstrom, V. Ramanathan, R. C. Cess, and G. G. Gibson, 1990: Seasonal variations of cloud radiative forcing derived from the Earth Radiation Budget Experiment. *J. Geophys. Res.,* **95,** 18 687–18 703.

Haywood, J. M., V. Ramaswamy, and B. J. Soden, 1999: Tropospheric aerosol climate forcing in clear-sky satellite observations over the oceans. *Science,* **283,** 1299–1303.

Hibler, W. D., III, 1979: A dynamic thermodynamic sea ice model. *J. Phys. Oceanogr.,* **9,** 817–846.

Horowitz, L. W., and Coauthors, 2003: A global simulation of tropospheric ozone and related tracers: Description and evaluation of MOZART, version 2. *J. Geophys. Res.,* **108,** 4784, doi:10.1029/2002JD002853.

Hunke, E. C., and J. K. Dukowicz, 1997: An elastic–viscous–plastic model for sea ice dynamics. *J. Phys. Oceanogr.,* **27,** 1849–1867.

Jones, P. D., and A. Moberg, 2003: Hemispheric and large-scale surface air temperature variations: An extensive revision and an update to 2001. *J. Climate,* **16,** 206–223.

——, M. New, D. E. Parker, S. Martin, and I. G. Rigor, 1999: Surface air temperature and its variations over the last 150 years. *Rev. Geophys.,* **37,** 173–199.

——, T. J. Osborn, K. R. Briffa, C. K. Folland, B. Horton, L. V. Alexander, D. E. Parker, and N. A. Rayner, 2001: Adjusting for sampling density in grid-box land and ocean surface temperature time series. *J. Geophys. Res.,* **106,** 3371–3380.

Jones, P. W., 1999: First- and second-order conservative remapping schemes for grids in spherical coordinates. *Mon. Wea. Rev.,* **127,** 2204–2210.

Kalnay, E., and Coauthors, 1996: The NCEP/NCAR 40-Year Reanalysis Project. *Bull. Amer. Meteor. Soc.,* **77,** 437–471.

Knutson, T. R., T. L. Delworth, I. M. Held, R. J. Stouffer, K. W. Dixon, D. Schwarzkopf, G. Stenchikov, and V. Ramaswamy, 2006: Assessment of twentieth-century regional surface temperature trends using the GFDL CM2 coupled models. *J. Climate,* in press.

Lin, S.-J., 2004: A "vertically Lagrangian" finite-volume dynamical core for global models. *Mon. Wea. Rev.,* **132,** 2293–2307.

Manabe, S., and R. J. Stouffer, 1996: Low-frequency variability of surface air temperature in a 1000-year integration of a coupled atmosphere–ocean–land surface model. *J. Climate,* **9,** 376–393.

——, ——, M. J. Spelman, and K. Bryan, 1991: Transient responses of a coupled ocean–atmosphere model to gradual

changes of atmospheric CO_2. Part I: Annual mean response. *J. Climate,* **4,** 785–818.

Milly, P. C. D., and A. B. Shmakin, 2002: Global modeling of land water and energy balances. Part I: The land dynamics (LaD) model. *J. Hydrometeor.,* **3,** 283–299.

Murray, R. J., 1996: Explicit generation of orthogonal grids for ocean models. *J. Comput. Phys.,* **126,** 251–273.

Norris, J. R., and C. B. Leovy, 1994: Interannual variability in stratiform cloudiness and sea surface temperature. *J. Climate,* **7,** 1915–1925.

Olivier, J. G. J., and Coauthors, 1996: Description of EDGAR Version 2.0: A set of global emission inventories of greenhouse gases and ozone-depleting substances for all anthropogenic and most natural sources on a per country basis and on $1° \times 1°$ grid. National Institute of Public Health and the Environment (RIVM) Rep. 771060 002, TNO-MEP Rep. R96/119, 171 pp.

Parker, D. E., C. K. Folland, and M. Jackson, 1995: Marine surface temperature: Observed variations and data requirements. *Climatic Change,* **31,** 559–600.

Randel, W. J., and F. Wu, 1999: A stratospheric ozone trends data set for global modeling studies. *Geophys. Res. Lett.,* **26,** 3089–3092.

Rayner, N. A., D. E. Parker, E. B. Horton, C. K. Folland, L. V. Alexander, D. P. Rowell, E. C. Kent, and A. Kaplan, 2003: Globally complete analyses of sea surface temperature, sea ice and night marine air temperature, 1871–2000. *J. Geophys. Res.,* **108,** 4407, doi:10.1029/2002JD002670.

Rosati, A., K. Miyakoda, and R. Gudgel, 1997: The impact of ocean initial conditions on ENSO forecasting with a coupled model. *Mon. Wea. Rev.,* **125,** 754–772.

Semtner, A. J., 1976: A model for the thermodynamic growth of sea ice in numerical investigations of climate. *J. Phys. Oceanogr.,* **6,** 27–37.

Steele, M., R. Morfley, and W. Ermold, 2001: PHC: A global ocean hydrography with a high-quality Arctic Ocean. *J. Climate,* **14,** 2079–2087.

Stouffer, R. J., 2004: Time scales of climate response. *J. Climate,* **17,** 209–217.

——, A. J. Weaver, and M. Eby, 2004: A method for obtaining pretwentieth century initial conditions for use in climate change studies. *Climate Dyn.,* **23,** 327–339.

——, and Coauthors, 2006: GFDL's CM2 global coupled climate models. Part IV: Idealized climate response. *J. Climate,* **19,** 723–740.

Talley, L. D., J. L. Reid, and P. E. Robbins, 2003: Data-based meridional overturning streamfunctions for the global ocean. *J. Climate,* **16,** 3213–3226.

Thompson, D. W. J., and J. M. Wallace, 2000: Annular modes in the extratropical circulation. Part I: Month-to-month variability. *J. Climate,* **13,** 1000–1016.

——, ——, and G. C. Hegerl, 2000: Annular modes in the extratropical circulation. Part II: Trends. *J. Climate,* **13,** 1018–1036.

Trenberth, K. E., and J. M. Caron, 2001: Estimates of meridional atmosphere and ocean heat transports. *J. Climate,* **14,** 3433–3443.

Winton, M., 2000: A reformulated three-layer sea ice model. *J. Atmos. Oceanic Technol.,* **17,** 525–531.

Wittenberg, A. T., A. Rosati, N.-C. Lau, and J. J. Ploshay, 2006: GFDL's CM2 global coupled climate models. Part III: Tropical Pacific climate and ENSO. *J. Climate,* **19,** 698–722.

Xie, P., and P. A. Arkin, 1997: Global precipitation: A 17-year monthly analysis based on gauge observations, satellite estimates, and numerical model outputs. *Bull. Amer. Meteor. Soc.,* **78,** 2539–2558.